POLITECNICO DI TORINO

Dipartimento di Ingegneria Meccanica e Aerospaziale

Corso di Laurea Magistrale in Ingegneria Aerospaziale

Tesi di Laurea Magistrale

Experimental characterization of the turbulent boundary layer over a flat plate

Relatore:
Prof. Renzo Arina

Candidato:
Riccardo Salis

Correlatori:
Prof. Domenic D'Ambrosio
Prof. Christophe Schram
Dr. Riccardo Zamponi

Anno accademico 2019/2020

von Karman Institute for Fluid Dynamics
Chaussée de Waterloo, 72
B-1640 Rhode-Saint-Genèse - Belgium

Short Training Report 2021

Experimental characterization of the turbulent boundary layer over a flat plate

Riccardo Salis

Supervisor: Prof. Christophe Schram
Advisor: Dr. Riccardo Zamponi

April 2021

A Mamma e Papà,
la mia più grande forza

Acknowledgments

First of all, I would like to thank my PoliTo supervisors, Professor Arina and Professor D'Ambrosio, who allowed me to start this experience abroad and followed my work during the STP period. I am very thankful to my VKI supervisor, Professor Schram, who welcomed me in the VKI Aeroacoustics Team since the first day and gave me some precious suggestions that enriched my project.

I am deeply grateful to my VKI advisor, Dr. Riccardo Zamponi. He introduced me to the experimental life in the best way possible, and he passed on his passion and positivity to me during the entire STP period. He always helped me for every problem and doubt, and encouraged me during the many experimental problems I had to overcome. My VKI journey would not have been as great as it was without his guidance.

I would like to thank my workmates Stefanie and Erica, who helped me during the experimental campaign and made my lab days more amusing. I also would like to thank Julien de Decker, who helped me a lot to solve technical problems during the experiments, and all the members of the VKI Aeroacoustics Team who gave me precious advices during our meetings.

I am really glad to have had my friend Martina as roomate during the Belgium journey. Her sympathy and kindness made this experience more enjoyable and funny. We shared the entire university life together, and our friendship has become even deeper after the VKI experience in Belgium. I could not ask for a better person to share the entire journey.

Turning now to the persons who accompanied and supported me during my university career, my first thought goes to my family. Mum, Dad and Mietta have guided me in this world since the beginning, and have given me the force to overcome every difficulty of my life. They made so many sacrifices for me without hesitation, and they supported me in every choice I made. I would not be the person I am without them. I am and I will be forever grateful to have the most beautiful family I could ever ask for.

A special thanks goes to my lovely girlfriend Lucia, who makes my life better since two years. She has always been supportive in every moment spent together, and in every decision I made for my career, even though that meant being apart. Her love makes my life so much happier every day, and I am so lucky to have her by my side.

A huge thank you is for my best friends Jacopo, Luca, Giorgio, Alberto, Stefania, Valentina, Martina, Luca, Antonio, Simone and Marta. Their joy and support brought me the serenity and happiness I needed to carry on in this long journey. Although it has been five years since I left home, our special bond never changed and they always look forward to celebrate me for my every homecoming. I am so thankful to have the most amazing friends of all-time.

Finally I would like to thank my Turin roomates Edoardo, Enrico and Alberto, and my university colleagues, who shared with me all the good and difficult moments of this journey. They made my university life crazy and exciting even in the moments of full-immersion study. I will always remember with joy all the great times spent together in these tough but incredible five years.

Abstract

Pressure fluctuations within a Turbulent Boundary Layer (TBL), which inevitably develops over a body immersed in a flow field, induce noise either by energizing the solid surface or with a direct contribution. The attenuation of this source of noise is particularly critical in aircraft and automotive industry, considering the increase of traffic and the extension of urban areas together with the rising public health concern. For this reason, the physical understanding of noise production and attenuation is becoming increasingly important in such engineering fields.

Studies devoted to understand the characteristics of the Wall-Pressure Spectra (WPS) in a TBL have been conducted over the years, leading to a development of statistical models for the wall-pressure fluctuations. Such models are commonly used as input for the determination of the structural response of the wall and the noise prediction in many engineering applications. However, they are heavily dependent upon empirical quantities, thus they can be tuned and improved basing on experimental databases for different flow conditions.

An experimental characterization of the turbulent boundary layer over a flat plate under zero pressure gradient has therefore been conducted in the present work. The aim of this project is to study the trend of the WPS in a turbulent boundary layer, in order to improve the physical understanding of the interaction between the grazing flow and the solid surface, and enrich the existing database in literature to promote the improvement of statistical models.

Experiments have been carried out in the WAABLIEF (Wind tunnel for the Aerodynamic and Acoustic study of Boundary Layers Including pressure gradient EFfects) facility at the von Karman Institute for Fluid Dynamics (VKI) in Rhode-Saint-Genèse, Belgium. The experimental campaign includes velocity and wall-pressure measurements by means of hot-wire anemometry and microphone-array measurements, respectively. Moreover, an innovative procedure for the calibration of the microphone array is proposed in this study. In addition, preliminary Particle Image Velocimetry (PIV) measurements have been conducted, in order to explore the possibility of using such a technique to provide additional information on the velocity field in the TBL over the flat plate.

In conclusion, the results obtained in this work constitute an extended database for velocity and pressure fields that offer the opportunity to validate and improve the statistical models available in literature.

List of Figures

List of Tables

List of symbols

Acronyms

B&K	Brüel & Kjær
DFT	Discrete Fourier Transform
FFT	Fast Fourier Transform
FOV	Field-Of-View
PIV	Particle Image Velocimetry
PSD	Power Spectral Density
PTU	Programmable Timing Unit
SPL	Sound Pressure Level
TBL	Turbulent Boundary Layer
TF	Transfer Function
TI	Turbulence Intensity
TKE	Turbulent Kinetic Energy
VKI	von Karman Institute
VPP	Peak-to-Peak Voltage
WAABLIEF	Wind tunnel for the Aerodynamic and Acoustic study of Boundary Layers Including pressure gradient EFfects
WPS	Wall-Pressure Spectra
ZPG	Zero Pressure Gradient

Greek symbols

α, β	Corcos model's constants	[-]
Γ	Cross-coherence funtion (single-sided)	[-]
γ	Ratio of specific heats at constant pressure and volume	[-]
γ_{wat}	Specific weight of water	[N/m^3]
δ	Boundary layer thickness	[m]
δ^*	Displacement thickness	[m]
θ	Momentum thickness	[m]
λ	Acoustic wavelength	[m]
ν	Flow kinematic viscosity	[m^2/s]
Π	Wake strength parameter	[-]

ρ	Density of the fluid	[kg/m^3]
τ	Shear stress	[Pa]
τ_c	Characteristic response-time of the hot-wire system	[s]
Φ	Power Spectral Density or auto-power spectrum (single-sided)	[Pa^2/Hz]
ω	Angular frequency	[rad/s]

Roman symbols

A	Cross-sectional area	[m^2]
a	Speed of sound	[m/s]
C	Constant of integration for the logarithmic law	[-]
C_1, C_2, C_3	Goody model's constants	[-]
c_f	Skin friction coefficient	[-]
d_p	Displacement on the image plane	[pixels]
E	Voltage	[V]
$\mathcal{F}$	Fourier Transform operator	
f	Frequency	[Hz]
H	Shape factor	[-]
h	Height of the water column in the manometer	[m]
j	Imaginary unit	[-]
k	Karman constant	[-]
k_B	Coefficient for hot-wire binormal velocity component	[-]
k_c	Ratio between angular frequency and convection velocity	[-]
k_T	Coefficient for hot-wire tangential velocity component	[-]
l	Side-length of the test section	[m]
M	Magnification factor	[mm/pixel]
m	Index for the frequency-domain discrete signal	[-]
N	Number of samples	[-]
n	Index for the time-domain discrete signal	[-]
P	Wall-pressure fluctuations in frequency domain	[Pa]
p	Flow pressure	[Pa]
q	Dynamic pressure	[Pa]
R	Specific gas constant for air	[J/(kg K)]
R_T	Ratio of the outer-to-inner-layer timescale	[-]
Re	Reynolds number	[-]
S	Cross-power spectrum (single-sided)	[Pa^2/Hz]
T	Temperature of the fluid	[K]
TF	Final transfer function (double-sided)	[Pa/V]
TF_1	Transfer function of step 1 (double-sided)	[-]
TF_2	Transfer function of step 2 (double-sided)	[Pa/V]
TI	Turbulence intensity	[-]
t	Time	[s]
U	Flow velocity	[m/s]

U_c	Convection velocity	[m/s]
u	Streamwise velocity component	[m/s]
u_τ	Friction velocity	[m/s]
v	Wall-normal velocity component	[m/s]
x	Streamwise direction or position	[m]
y	Wall-normal direction or position	[m]
z	Spanwise direction or position	[m]

Subscripts and superscripts

$\bar{\ }$	Mean value of the quantity
$'$	Fluctuating value of the quantity
$+$	Normalized in wall variables
$*$	Normalized with outer-layer parameters
$\tilde{\ }$	Related to the intersection point in Bradshaw's method
∞	Related to an inlet quantity
$\circ$	Related to a total quantity
0	Related to ambient conditions
θ	Related to the momentum thickness
a	Related to the acoustic field
B	Related to the hot-wire binormal direction
cal	Related to the calibrator B&K microphone
cr	Related to the critical value for boundary layer transition
e	Related to an external quantity outside the boundary layer
ele	Related to the electret microphone
fan	Related to the axial fan of the facility
m	Related to the m-th element of the frequency-domain discrete signal
max	Related to the maximum frequency of interest
N	Related to the hot-wire normal direction
n	Related to the n-th element of the time-domain discrete signal
out	Related to the outlet of the pressurized nozzle
pp	Related to the wall-pressure fluctuations
Re	Related to the Reynolds shear stress
ref	Related to the reference B&K microphone
rfc	Related to the reference value of the quantity
rms	Root mean square of the quantity
s	Related to the sampling parameters
sc	Related to the settling chamber
T	Related to the hot-wire tangential direction
u	Related to the streamwise velocity component
$visc$	Related to the viscous shear stress
w	Related to a wall quantity
x	Related to the streamwise position

Contents

Chapter 1

Introduction

1.1 Document outline

This document is related to the final Master's Degree thesis of the Aerospace Engineering course at Politecnico di Torino. The entire work has been carried out during a five-month Short Training Program at the von Karman Institute for Fluid Dynamics (VKI) in Rhode-Saint-Genèse, Belgium. Precisely, the experimental campaign took place in the WAABLIEF (Wind tunnel for the Aerodynamic and Acoustic study of Boundary Layers Including pressure gradient EFfects) facility of the VKI, which is a particularly designed acoustic wind tunnel where the test section is located in a semi-anechoic room.

1.1.1 The von Karman Institute for Fluid Dynamics

VKI is a non-profit international educational and scientific organization, hosting three departments (Aeronautics and Aerospace, Environmental and Applied Fluid Dynamics, and Turbomachinery and Propulsion) [1]. It provides post-graduate education in fluid dynamics (Research Master in Fluid Dynamics, which is a Master-after-Master level and also known as the former "VKI Diploma Course", Doctoral Programme, Short Training Program and lecture series) and encourages "training in research through research".

The von Karman Institute undertakes and promotes research in the field of fluid dynamics. Extensive research on experimental, computational and theoretical aspects of gas and liquid flows is carried out at the VKI under the direction of the faculty and research engineers, sponsored mainly by governmental and international agencies as well as industries. Furthermore, this Center of Excellence operates about fifty different wind tunnels, turbomachinery and other specialized test facilities; some of them being unique. The facilities of the Institute are renowned and VKI is recognized as a world-class research center of excellence by its peers.

Figure 1.1: The von Karman Institute for Fluid Dynamics.

1.1.2 Structure of the report

The present work is constituted by seven main parts:

1. A first introduction has the aim to explain the considered problem. A brief explication on the importance of noise prediction and reduction, especially in aircraft and automotive industry, is given, and the experimental campaign of the present work is introduced.

2. The second section contains the theoretical background on which the experimental campaign is based on. In particular, an introduction of TBL parameters is presented, along with elements of acoustic propagation. Furthermore, some TBL statistical models useful to be compared with the experimental database are shown.

3. The third part of the document is focused on the experimental set-up and the measurement strategies. Calibrations of several instruments, key element of the measuring chain, are explained in detail, as well as set-up and acquisition chain needed during the experimental campaign.

4. The fourth part is dedicated to the post-processing of the velocity measurements, both for inlet velocity and velocity field over the flat plate. The aim of this section is to retrieve the TBL characteristics that are useful for the wall-pressure spectra (WPS) analysis.

5. The fifth chapter contains the wall-pressure analysis, focusing on the results

obtained from calibration and wind tunnel acquisitions of the microphone array and the comparison with some statistical models available in literature.

6. The sixth section describes the preliminary test of Particle Image Velocimetry (PIV) measurements. This section will be important for a future PIV campaign in the WAABLIEF facility, as it shows the feasibility of such technique in this facility and provides valuable informations about the set-up and the post-processing of the data acquired.

7. The seventh and latter section of the work reports the conclusions drawn from the results of the experimental campaign, and provides some ideas for future developments and improvements to the present work.

1.2 Problem explanation

The Turbulent Boundary Layer (TBL), whose characteristics are particularly important in many fields, such as aerospace or automotive industry, is ubiquitous in engineering applications. In particular, pressure fluctuations within the turbulent boundary layer draw the attention of engineers and scientists, since they provide the indirect information regarding the interaction between the vortical structures and the solid surface, which cause flow-induced noise or vibration [2]. For this reason, the physical understanding of noise production and attenuation is becoming increasingly important in such engineering fields.

Pressure fluctuations over an immersed body induce noise either by energizing the solid surface or with a direct contribution as a quadrupole [3]. The attenuation of this source of noise is particularly critical in aircraft and automotive industry, considering the increase of traffic and the extension of urban areas together with the rising public health concern. Indeed, wall-pressure fluctuations that are associated to the vortical structures developing in the turbulent boundary layer induce structure vibrations, which in turn generate noise inside the cabin [2]. This noise transmission issue has become even more severe with the increasing pressure on manufacturers and industries for lightweight structures and eco-friendly products. This has led not only to the use of thinner panels but also of new composite materials, whose mechanical and vibrational characteristics need to be accounted in the early design phase. A fortiori, the acoustic comfort of passengers must be an important concern for the development of transportation vehicles.

Studies devoted to understand the characteristics of the WPS in a turbulent boundary layer have been conducted over the years. Wall-pressure spectra of a TBL, despite being random, display distinct features, enabling the development of statistical models for the wall-pressure fluctuations. Such models are commonly used as input for the determination of the structural response of the wall and the noise prediction in many engineering applications, such as ground or air vehicle cabin noise, for instance [2]. Indeed, they yield the wall-pressure spectra as a function of the TBL statistical quantities, such as mean velocity and turbulence intensity. However, they are heavily dependent upon empirical quantities, thus they can be tuned and improved basing on experimental databases for several flow conditions.

An experimental characterization of the turbulent boundary layer over a flat plate under zero pressure gradient has therefore been conducted in the present work. The experimental campaign includes velocity and wall-pressure measurements by means of hot-wire anemometry and microphone-array measurements, respectively. Moreover, an innovative calibration procedure for the microphone array is proposed in this study, and turned out to be quite challenging, revealing some ideas for future improvements. In addition, preliminary Particle Image Velocimetry (PIV) measurements have been conducted, in order to explore the possibility of using such a technique to provide additional information on the velocity field in the turbulent boundary layer over the flat plate.

1.3 Aim of the project

The aim of this project is to study the trend of the WPS in a turbulent boundary layer, in order to improve the physical understanding of the interaction between the grazing flow and the solid surface, and enrich the existing database in literature to promote the validation and improvement of statistical models of wall-pressure fluctuations. Indeed, since TBL models typically include several empirical constants, the generated database could play a key role in the fine-tuning and development of such models.

As the models are function of various TBL parameters, velocity measurements are needed in order to retrieve the flow velocity field over the flat plate, which means to have the possibility of comparing such models with the generated WPS database. After the TBL statistical quantities have been derived, parameters that characterize the wall-pressure fluctuactions are retrieved and finally compared with some statistical models of the literature.

At last, another important goal of the present work is to show the successful PIV preliminary test that has been conducted in the WAABLIEF facility. The material collected in this analysis is precious for a future PIV campaign: indeed, some valuable informations to obtain an efficient set-up are present, and promising results for the flow velocity field, which are very encouraging for the future, are shown.

Chapter 2

Theoretical background

2.1 Introduction to the boundary layer

When a body is immersed in a flow, the viscosity effect generates a development of the boundary layer in the vicinity of the wall. Within this very thin region, viscous effects are preponderant: the wall implies the no-slip condition to the flow, while by going towards higher distances from the wall the velocity asymptotically tends to the external velocity outside the boundary layer. Viscosity effects are concentrated in the boundary layer, leading to a flow field characterized by velocity gradients $\partial u/\partial y$ greater as the distance from the wall decreases, while the inviscid outer flow is not influenced by such effects.

Considering the simple case of bidimensional, incompressible, steady flow, Navier-Stokes equations for mass and momentum conservation can be written as:

$$\frac{\partial u}{\partial x} + \frac{\partial v}{\partial y} = 0 \tag{2.1}$$

$$u\frac{\partial u}{\partial x} + v\frac{\partial u}{\partial y} = -\frac{1}{\rho}\frac{\partial p}{\partial x} + \nu\left(\frac{\partial^2 u}{\partial x^2} + \frac{\partial^2 u}{\partial y^2}\right) \tag{2.2}$$

$$u\frac{\partial v}{\partial x} + v\frac{\partial v}{\partial y} = -\frac{1}{\rho}\frac{\partial p}{\partial y} + \nu\left(\frac{\partial^2 v}{\partial x^2} + \frac{\partial^2 v}{\partial y^2}\right) \tag{2.3}$$

By following the approximation introduced by L. Prandtl in 1904, based on the comparison between the orders of magnitude of each term in the Navier-Stokes equations, the latter can be simplified to yield approximate solutions for the boundary layer case [4]:

$$\frac{\partial u}{\partial x} + \frac{\partial v}{\partial y} = 0 \tag{2.4}$$

$$u\frac{\partial u}{\partial x} + v\frac{\partial u}{\partial y} = -\frac{1}{\rho}\frac{\partial p}{\partial x} + \nu\frac{\partial^2 u}{\partial y^2} \tag{2.5}$$

$$\frac{\partial p}{\partial y} = 0 \tag{2.6}$$

With boundary conditions:

$$\begin{cases} y = 0 : & u = 0, \;\; v = 0 \\ y \to \infty : & u = U_e \end{cases} \tag{2.7}$$

In particular, Equation (2.6) provides an important information about boundary layer flows: the static pressure p remains constant along the wall-normal direction, i.e. $p = p_e(x)$.

Furthermore, if the simplest case of boundary layer along a flat plate with zero incidence is considered, then the static pressure remains constant also along the streamwise direction, that is the Zero Pressure Gradient (ZPG) case $dp_e/dx = 0$, which means that the velocity of the potential flow is constant. In this case, the boundary layer equations (2.4) and (2.5) become:

$$\frac{\partial u}{\partial x} + \frac{\partial v}{\partial y} = 0 \tag{2.8}$$

$$u\frac{\partial u}{\partial x} + v\frac{\partial u}{\partial y} = \nu\frac{\partial^2 u}{\partial y^2} \tag{2.9}$$

Depending on several factors, the boundary layer can be in laminar or turbulent regime:

- The laminar regime is characterized by a very smooth and regular development of the flow over the wall. This configuration has lower values of wall shear stress than the turbulent regime, but it is less stable and more prone to flow separation under strong adverse pressure gradients.
- The turbulent regime is the most prevalent in engineering applications. This configuration contains streaks and swirls that get deformed in a chaotic, irregular and unpredictable way. These characteristics lead to vorticity fluctuations that yield an unsteady and nonlinear flow: for this reason, turbulent flows are usually described by means of a statistical approach.

A typical transition from laminar to turbulent regime in the boundary layer over a flat plate is depicted in Figure 2.1.

The main parameter governing this mechanism is the local Reynolds number, defined as:

$$Re_x = \frac{U_e\, x}{\nu} \tag{2.10}$$

Where U_e is the external velocity outside the boundary layer, x is the streamwise position and ν is the flow kinematic viscosity. For a flat plate in normal flow conditions with ZPG, transition to turbulent regime occurs for Re_x greater than $5 \cdot 10^5$ [4]. However, boundary layer transition depends also on other factors that can anticipate or delay its occurence: for istance, tripping and rough elements over the solid surface can force transition to turbulence before reaching the canonical critical value.

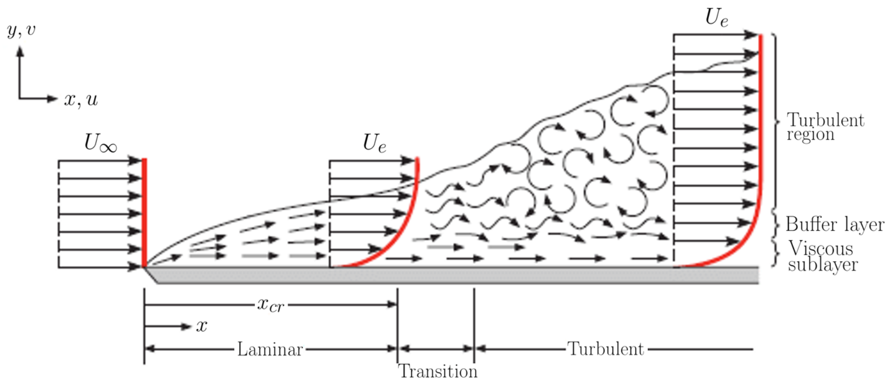

Figure 2.1: Evolution of the boundary layer over a flat plate with zero incidence [5] (original source [6]).

2.1.1 Boundary layer parameters

In a boundary layer flow, several parameters can be retrieved in order to properly characterize and classify the flow field. Definition and description of these quantities are briefly discussed below.

Boundary layer thickness

The boundary layer thickness δ represents the limit between viscous and outer flow, i.e. the physical contour that defines the boundary layer region. However, as the transition from boundary layer flow to inviscid flow takes place continuously, it is impossible to state a precise boundary definition [4]. For this reason, the definition of the boundary layer thickness is arbitrarily given, usually by considering the distance from the wall where the velocity reaches the 99% of the outer velocity U_e.

This parameter is dependent on streamwise position x: indeed, as the distance from the leading edge of the body gets larger, more fluid particles are influenced by viscosity effects, leading to an increase of the boundary. Thickness $\delta(x)$ turns out therefore to be a monotonically increasing function of x. A schematic indication of the boundary layer thickness is shown in Figure 2.2.

Displacement thickness

A more meaningful and interpretable measure for the thickness of the boundary layer is the displacement thickness δ^*, defined as [4]:

$$\delta^* = \int_0^\infty \left(1 - \frac{\bar{U}(x,y)}{U_e}\right) dy \tag{2.11}$$

Where $\bar{U}(x,y)$ is the mean velocity profile.

This quantity is an indicator of how far the streamlines of the outer flow are influenced by the boundary layer, and represents the mass flow lost in the boundary layer

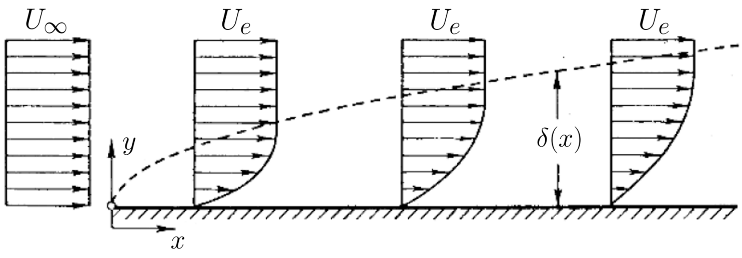

Figure 2.2: Schematic representation of the boundary layer thickness developing over a flat plate [4].

due to viscosity effects. An illustration of the displacement thickness is given in Figure 2.3: the two shaded areas in the sketch must be equivalent if a distance from the wall equal to δ^* is considered.

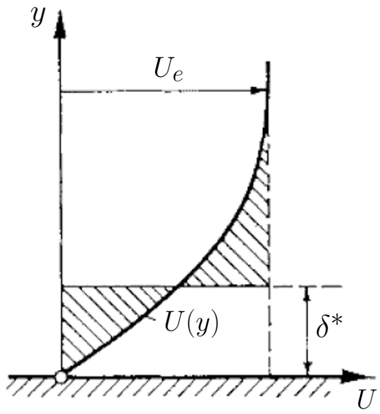

Figure 2.3: Schematic representation of the displacement thickness of the boundary layer [4].

Momentum thickness

The momentum thickness θ is another important parameter for the boundary layer. This quantity is indicative of the momentum lost in the boundary layer due to viscosity effects, and is defined as [4]:

$$\theta = \int_0^\infty \frac{\bar{U}(x,y)}{U_e}\left(1 - \frac{\bar{U}(x,y)}{U_e}\right) dy \tag{2.12}$$

Shape factor

The shape factor H is simply the ratio between displacement and momentum thickness:

$$H = \frac{\delta^*}{\theta} \tag{2.13}$$

This quantity is essential to classify the nature of the boundary layer: indeed, for the case of flat plate at zero incidence, it assumes a value of 2.59 in laminar regime while it decreases to about 1.4 for a turbulent boundary layer [4].

Friction velocity

The friction velocity u_τ is a parameter that expresses the wall shear stress in velocity terms, and since it represents the characteristic velocity for turbulent flows, it is often used as a scaling parameter for TBL velocity profiles. The definition of this quantity is formulated as [4]:

$$u_\tau = \sqrt{\frac{\tau_w}{\rho}} \tag{2.14}$$

With τ_w as the wall shear stress, which can be written as follows:

$$\tau_w = \frac{1}{2}\rho\, U_e^2\, c_f \tag{2.15}$$

Where c_f is the skin friction coefficient and ρ is the density of the fluid.

2.1.2 Turbulent boundary layer structure

Since velocity profiles in a boundary layer are dependent on several parameters, it is convenient to have an universal profile to be referred to. In the laminar case, the compactness of the velocity profile is obtained by using δ and U_e for the normalization of coordinate y and mean velocity $\bar{U}(x, y)$, respectively [7]. However, this normalization does not lead to an universal profile for a turbulent boundary layer.

As the wall shear stress plays a very important role in a TBL, it is found that turbulent profile curves form a single-parameter family of the skin friction coefficient, i.e. an universal curve is obtained by rescaling the variables with a factor involving c_f. The friction velocity u_τ therefore turns out to be the perfect parameter for the normalization of turbulent velocity profiles. The dimensionless wall variables are defined as:

$$y^+ = \frac{y\, u_\tau}{\nu} \tag{2.16}$$

$$U^+ = \frac{\bar{U}}{u_\tau} \tag{2.17}$$

The trend of the universal turbulent profile curve in shown in Figure 2.4. As can be seen the TBL presents a multilayer structure, which is principally constituted by two regions:

1. The inner layer, which typically represents 10-20% of the boundary layer thickness, is the region closest to the wall, as well as the dynamically most active part in terms of Turbulent Kinetic Energy (TKE) production. In this region, it is a good approximation to assume that the total shear stress, sum of viscous and Reynolds shear stress, is constant along the wall-normal direction [10]:

$$\tau(y) = \tau_{visc} + \tau_{Re} = \text{const} = \tau_w \tag{2.18}$$

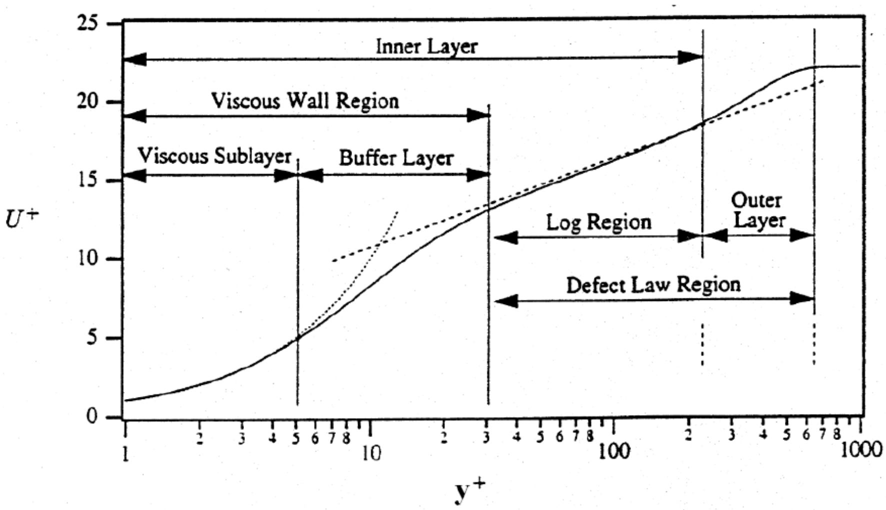

Figure 2.4: Universal curve for the velocity profile in a turbulent boundary layer [8] (original source [9]).

This expression leads to the explicit formulations of the so-called "Law of the Wall" $U^+ = f(y^+)$, illustrated in Figure 2.4.

2. The outer layer is the external part of the boundary layer. In this region, the velocity profile tends to the external velocity U_e outside the TBL.

As can be noted in Figure 2.4, the inner layer is divided in three other layers where the Law of the Wall assumes different formulations, depending on the characteristics of the subregion:

1. The viscous sublayer ($y^+ \leq 5$) is the region closest to the wall, where the viscous stress dominates over the Reynolds stress. In this case, τ_{Re} in Equation (2.18) can be neglected, leading to this relation for the velocity profile:

$$U^+ = y^+ \tag{2.19}$$

2. The logarithmic layer ($30 \leq y^+ \leq 300$) is the outer region of the inner layer, where the viscous stress can be neglected compared to the turbulent shear stress. In this case, the Law of the Wall assumes a different expression:

$$U^+ = \frac{1}{k}\ln(y^+) + C \tag{2.20}$$

Where $k = 0.41$ is the Karman constant and $C = 5$ is the constant of integration for smooth walls [4].

3. The buffer layer ($5 < y^+ < 30$) is the region that links up viscous sublayer and logarithmic layer, where both viscous and turbulent stress are comparable

and where the peak production and dissipation of TKE occur. In this case, an expression for the Law of the Wall is proposed by Spalding [11]:

$$y^+ = U^+ + e^{-kC}\left[e^{kU^+} - 1 - kU^+ - \frac{(kU^+)^2}{2} - \frac{(kU^+)^3}{6}\right] \tag{2.21}$$

Which provides a smooth transition of the velocity profile from the viscous sublayer to the logarithmic layer. Indeed, the second term in Equation (2.21) is negligible in the viscous sublayer, obtaining Equation (2.19), while in the logarithmic layer the dominant term is the exponential and the expression becomes $y^+ \approx e^{-kC}e^{kU^+}$, which can be traced back to Equation (2.20) [10].

Moreover, in 1956 Coles [12] introduced a combination of two universal functions to describe the velocity profile within the so-called defect law region, which includes logarithmic and outer layer, as can be seen in Figure 2.4. One is the logarithmic law expressed in Equation (2.20), while the other is called the "Law of the Wake", leading to the following relation for the defect law region:

$$U^+ = \frac{1}{k}\ln(y^+) + C + \frac{2\Pi(x)}{k}\sin^2\left(\frac{y}{\delta}\cdot\frac{\pi}{2}\right) \tag{2.22}$$

Where $\Pi(x)$ is called the wake strength parameter, which is computed by solving the following equation in implicit form:

$$2\Pi - \ln(1+\Pi) = k\frac{U_e}{u_\tau} - \ln\left(\frac{\delta^* U_e}{\nu}\right) - kC - \ln(k) \tag{2.23}$$

This parameter is dependent on momentum Reynolds number and asymptotically tends to a constant value equal to about 0.55 for $Re_\theta > 5000$, as shown in Figure 2.5 [10].

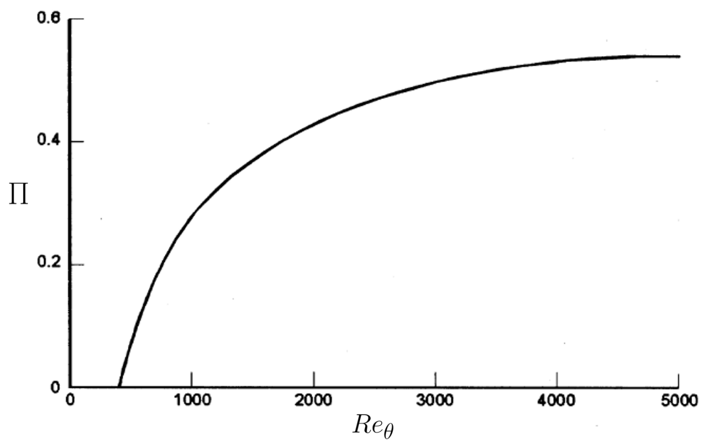

Figure 2.5: Variation of the wake strength parameter Π with Reynolds number Re_θ [10].

2.2 Elements of acoustic propagation

Sound is a pressure perturbation p' that propagates through a medium as a longitudinal acoustic wave by means of adiabatic compression and decompression, leading to energy propagation. A schematic view of acoustic wave propagation is shown in Figure 2.6.

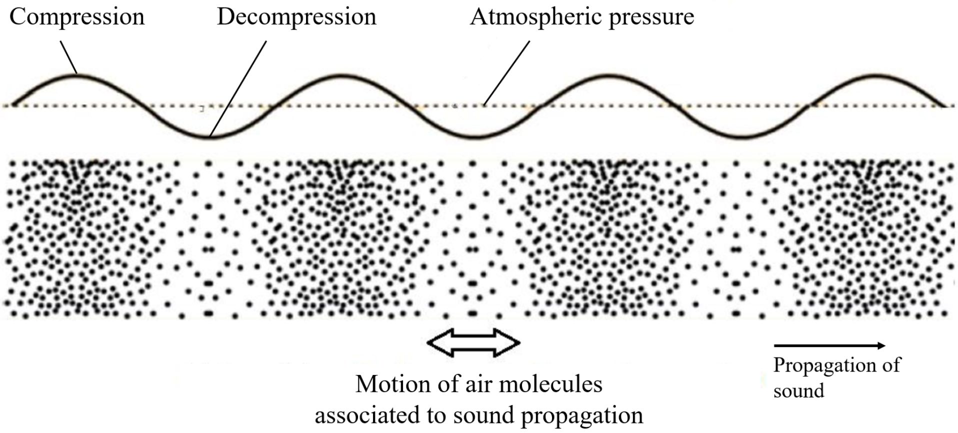

Figure 2.6: Schematic representation of sound wave propagation [13].

The transmission medium can be a gas or a liquid, such as air and water, or even a solid. Acoustic waves propagate with a characteristic speed of sound that depends on the medium and its temperature: for istance, in dry air at 20 °C it is equal to 344 m/s, while in water the typical value is 1500 m/s for the same environmental conditions [14].

For harmonic pressure fluctuations, the typical range of frequency perceived by the human ear is comprised between 20 Hz and 20 kHz, with a maximum sensitivity of the ear at mid-range frequencies around 3 kHz.

2.2.1 Sound Pressure Level

As the levels of sound pressure are comprised in a very wide range of values, it is convenient to use a logarithmic scale to measure sound levels referred to a reference value. The Sound Pressure Level (SPL) in decibels is therefore defined by the following relation [14]:

$$\mathrm{SPL} = 20\log_{10}\left(\frac{p'_{rms}}{p_{rfc}}\right) \tag{2.24}$$

Where p'_{rms} is the root mean square of the acoustic pressure fluctuations p', while p_{rfc} is the reference value of sound pressure that corresponds to the threshold of hearing. The latter is dependent on the transmission medium in which the acoustic waves are propagating: for example, the reference pressure is $p_{rfc} = 2 \cdot 10^{-5}$ Pa in air and $p_{rfc} = 2 \cdot 10^{-6}$ Pa in other media.

The threshold of pain is the sound level that the human hearing can only endure for a very short period of time without damaging the hearing, and is represented by a SPL equal to 140 dB. The range of human hearing can therefore assume values of SPL from 0 to 140 dB.

2.2.2 Order of magnitude estimations

Acoustic waves can be considered as small perturbations propagating in a transmission medium. This implies that second order effects can be neglected, and therefore the acoustic variables satisfy the linearization of the equations of motion [14].

In order to justify this statement, it is useful to give an example of the orders of magnitude in air propagation. Considering the threshold of pain, which is the maximum sound level of interest for human hearing, a SPL of 140 dB corresponds in air to pressure fluctuations of $p'_{rms} = 200$ Pa. If this value is compared to the typical atmospheric pressure of $p_0 = 10^5$ Pa, the result is:

$$\frac{p'_{rms}}{p_0} = 2 \cdot 10^{-3} \ll 1 \tag{2.25}$$

The order of magnitude of density fluctuations can be retrieved by introducing the relation between pressure and density fluctuations and the expression of the speed of sound a_0 at ambient conditions, respectively:

$$p' = a_0^2\, \rho' \tag{2.26}$$

$$a_0 = \sqrt{\gamma \frac{p_0}{\rho_0}} \tag{2.27}$$

Where γ is the ratio of specific heats at constant pressure and volume. The corresponding density fluctuations ρ'/ρ_0 are therefore obtained:

$$\frac{\rho'}{\rho_0} = \frac{p'}{\gamma\, p_0} \leq 10^{-3} \ll 1 \tag{2.28}$$

From Relations (2.25) and (2.28) it can be seen that the approximation of small pertubations is suitable for sound propagation, and therefore the linearized equations of motion can be used to describe the acoustic field.

Moreover, as the acoustic wavelength λ is the sound characteristic length, the acoustic Reynolds number is thus defined as:

$$Re_a = \frac{\lambda\, a_0}{\nu} \tag{2.29}$$

Which represents the ratio between inertial and viscous forces. Some values of this parameter in the range of frequency of the human ear are presented in Table 2.1 for the case of air propagation.

From Table 2.1, it is clear that inertial forces are dominant over the viscous forces as $Re_a \gg 1$. This means that viscous effects are relevant only for large distances of

f [Hz]	Re_a [-]
20	$4 \cdot 10^8$
10^3	$8 \cdot 10^6$
10^4	$8 \cdot 10^5$
$2 \cdot 10^4$	$4 \cdot 10^5$

Table 2.1: Acoustic Reynolds number for several frequencies for the case of air propagation.

acoustic propagation, i.e. the dissipation mechanism occurs after a significant number of cycles of the sound wave. In addition, since Re_a decreases as the frequency increases, it follows that high-frequency acoustic waves are damped faster than low-frequency ones. In conclusion, acoustic propagation can be considered as an isentropic field.

2.3 Wall-pressure spectra models

Within the turbulent boundary layer, the interaction between pressure fluctuations associated to the vortical structures and the solid wall of the body induces surface vibration, which in turn leads to sound production and radiation [2]. For this reason, noise production is closely linked to wall-pressure fluctuations. However, as wall-pressure fluctuations have a random behaviour, its determination requires a spectral analysis.

Consequently, it is appropriate to introduce the Fourier Transform $\mathcal{F}$ of the time-domain wall-pressure fluctuations, in order to obtain the spectrum in frequency domain. For a discrete one-point time-series of finite duration acquired in a fixed position in space, the Discrete Fourier Transform (DFT) of the n-th element of the time-series is defined as [15]:

$$P_m(\omega) = \mathcal{F}(p'_n(t)) = \frac{1}{2\pi} \sum_{n=0}^{N-1} p'_n(t)\, e^{-j\frac{2\pi}{N}mn} \tag{2.30}$$

Where $\omega = 2\pi f$ is the angular frequency, m and n are respectively the index for the frequency-domain and time-domain discrete signal, j is the imaginary unit and N is the number of samples.

A more significant parameter for spectral analysis is the Power Spectral Density (PSD) of wall-pressure fluctuations $\Phi_{pp}(\omega)$, also called as auto-power spectrum, which is determined by the following relation:

$$\Phi_{pp}(\omega) = \frac{\Delta t}{N} \left|P(\omega)\right|^2 \tag{2.31}$$

Where Δt is the sampling interval. By defining a coordinate system for streamwise and spanwise direction (x, z) centered in one point of the wall-pressure field, the cross-power spectrum $S_{pp}(x, z, \omega)$ between the point considered and another point on the surface can be factorized as [2]:

$$S_{pp}(x, z, \omega) = \Phi_{pp}(\omega)\, \Gamma_{pp}(x, z, \omega) \tag{2.32}$$

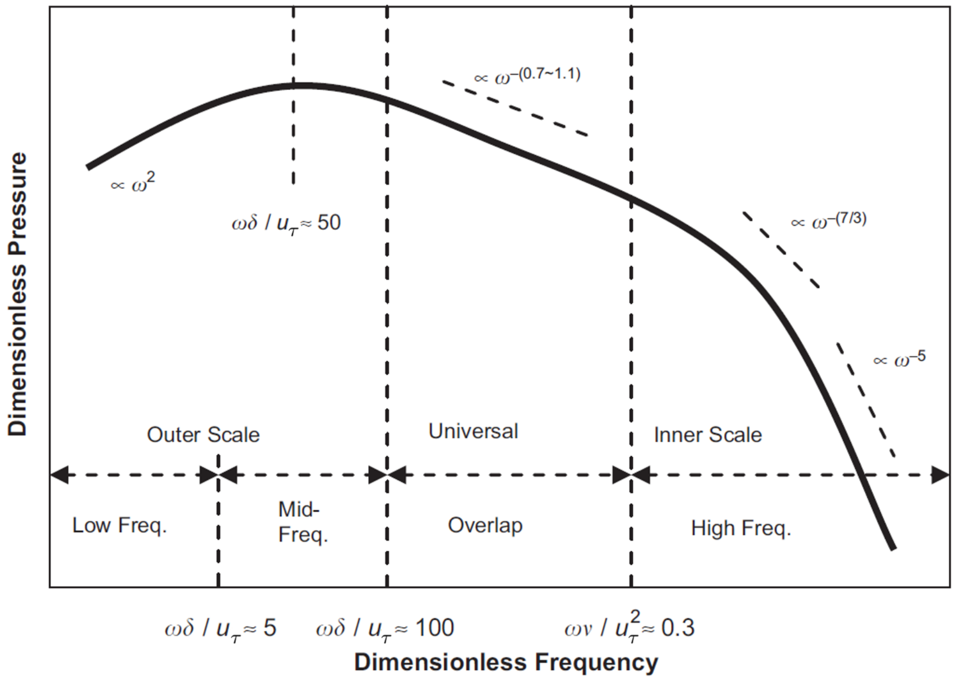

Figure 2.7: General auto-power spectrum characteristics in a TBL at different frequency regions [16].

Where $\Gamma_{pp}(x, z, \omega)$ is the cross-coherence function between the two points.

As in the case of TBL velocity profiles, scaling is a fundamental technique to predict the WPS generated in a turbulent boundary layer. During the years, several researchers have tried to find a single scaling that leads to a WPS collapse at all frequencies with different Reynolds numbers. However, no satisfactory single scaling has been found, but WPS collapse turned out to be reached using different scales (with outer- and inner-layer parameters) in four different frequency regions, which are defined as a function of angular frequency ω [16].

The general spectral characteristics are shown in Figure 2.7 and summarized as follows:

1. In the low-frequency region ($\omega\delta^*/U_e \leq 0.03$ or $\omega\delta/u_\tau \leq 5$) the dimensionless auto-power spectrum varies as ω^2. In this part, outer-layer parameters δ^* and U_e are used to scale angular frequency and WPS, leading to the dimensionless quantities $\omega\delta^*/U_e$ and $\Phi_{pp}(\omega)\, U_e/(\tau_w^2\, \delta^*)$, respectively.

2. In the mid-frequency region ($5 \leq \omega\delta/u_\tau \leq 100$) the same scaling of the low-frequency region can be used. In this range, a spectral peak is present approximately at $\omega\delta/u_\tau = 50$.

3. In the universal range ($100 \leq \omega\delta/u_\tau \leq 0.3\, u_\tau\delta/\nu$), also called as overlap region, both inner- and outer-scale can be used to obtain WPS collapse. This region

exists when $u_\tau \delta/\nu > 333$, and WPS trend may vary as $\omega^{-0.7}$ and $\omega^{-1.1}$, according to Goody [17] and Smol'yakov [18] respectively.

4. In the high-frequency region ($\omega\nu/u_\tau^2 \geq 0.3$) the dimensionless auto-power spectrum varies from ω^{-1} to ω^{-5}. Since in this region the WPS is influenced by viscosity, it is opportune to use inner-layer parameters ν and u_τ as scaling factors, leading to the dimensionless quantities $\omega\nu/u_\tau^2$ and $\Phi_{pp}(\omega)\, u_\tau^2/(\tau_w^2\, \nu)$ [16].

According to Goody [17], the inner-layer scaling at high frequencies shows general agreement in literature on auto-power spectrum collapse. However, the WPS collapse in low- and mid-frequency ranges with the outer-layer scaling is more complicated to obtain. Several researchers developed WPS semi-empirical models to find the proper outer-scale to collapse the spectra at low frequencies. In the present work two models, in which the pressure gradient is not taken into account, are considered:

1. In 1998, Howe [19] reported a model based on data collected by Chase [20], that is the so-called Chase-Howe's model:

$$\frac{\Phi_{pp}(\omega)\, U_e}{\tau_w^2\, \delta^*} = \frac{2\,\omega^{*2}}{\left(\omega^{*2} + 0.0144\right)^{3/2}} \tag{2.33}$$

   Where $\omega^* = \omega\delta^*/U_e$ is the dimensionless angular frequency scaled with outer-layer parameters. The factor 2 in the numerator is present here to be consistent with the single-sided computation of $\Phi_{pp}(\omega)$ used in this work. This model describes the essential features of the auto-power spectrum, despite being less complex than a more general model [17].

2. In 2004, Goody [17] used Equation (2.33) to develop a modified form that contemplates the Reynolds number effect through the ratio R_T of the outer-to-inner-layer timescale, defined as:

$$R_T = \frac{\delta/U_e}{\nu/u_\tau^2} \tag{2.34}$$

   Goody's model uses the boundary layer thickness δ for WPS scaling, but the model can be reformulated using the displacement thickness δ^*, as its computation is usually more accurate [2]. Using the relation $\delta^* = \delta/8$ that can be obtained for a $1/7^{\text{th}}$ power law canonical TBL velocity profile, Goody's model is formulated as:

$$\frac{\Phi_{pp}(\omega)\, U_e}{\tau_w^2\, \delta^*} = \frac{C_2\,\omega^{*2}}{\left(\omega^{*0.75} + C_1\right)^{3.7} + \left(C_3\,\omega^*\right)^7} \tag{2.35}$$

   Where $C_1 = 0.105$, $C_2 = 4.8$ and $C_3 = 3.76\, R_T^{-0.57}$.

In literature, statistical models to predict the cross-coherence function $\Gamma_{pp}(x, z, \omega)$ of wall-pressure fluctuations also exist. This function relate two different measurement points separated by a longitudinal distance x and a transversal distance z.

An example of model for the cross-coherence function is given by Corcos [21]. In 1964, he proposed a model that assumes spatial decays in both streamwise and spanwise directions [22]:

$$\Gamma_{pp}(x, z, \omega) = e^{-\alpha k_c |x|}\, e^{-\beta k_c |z|}\, e^{j k_c |x|} \tag{2.36}$$

Where $k_c = \omega/U_c$ is the ratio between the angular frequency and the convection velocity, while α and β are constants related to streamwise and spanwise correlation lengths respectively. This model assumes a constant phase shift in the spanwise direction and a statistical independence between the correlations lengths [2].

In Equation (2.36), α and β are revised by Blake (1986) [23] such that $\alpha = 0.116$ for smooth walls, $\alpha = 0.32$ for rough walls, and $\beta = 0.7$ for smooth and rough walls. Regarding the convection velocity U_c, this can be modelled with the outer-layer scaling by using the model proposed in 2006 by Smol'yakov [24]:

$$\frac{U_c}{U_e} = \frac{1.6\,\omega^*}{1 + 16\,\omega^{*2}} + 0.6 \tag{2.37}$$

All the models presented above will be therefore used to see the agreement with the experimental results obtained in the present work from microphone-array measurements. This analysis represents an opportunity to validate and improve the WPS models of the literature.

Chapter 3

Experimental set-up and measurement strategies

3.1 WAABLIEF facility

The experimental campaign took place in the WAABLIEF facility of the VKI, which is an open-circuit, suction-type, low-speed wind tunnel where the test section is confined to a semi-anechoic room. The acoustically isolated chambers sorrounding the test section and the diffuser make this unique wind tunnel particularly suitable for aeroacoustic studies. The schematic view of the facility is presented in Figure 3.1.

The wind tunnel incorporates an air inlet, a circular cross-section settling chamber fitted with honeycomb and meshes, and an axisymmetric 9:1 contraction leading to a squared (0.25 x 0.25) m^2 test section with a length of 2 meters. This facility is especially suited for research projects and laboratory training in turbulent boundary layers, three-dimensional velocity measurements and, with the addition of a smoke generator and of an air exhaust to outside, laser sheet flow visualizations and quantitative optical techniques, such as Laser Doppler Velocimetry and PIV. The latter feature is possible

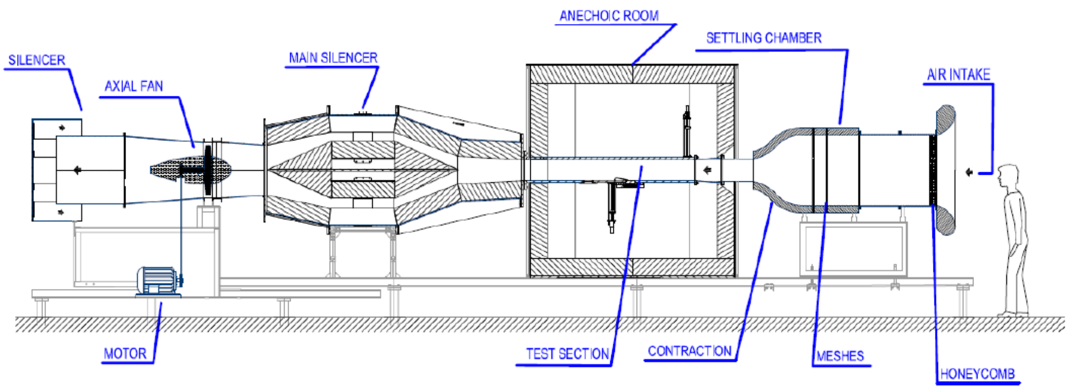

Figure 3.1: Schematic view of the WAABLIEF facility [8].

thanks to the presence of three plexiglas walls (side walls and top wall) in the test section.

The air is sucked through the circular bell-mouth inlet, immediately after which the honeycomb grid is located. The latter has the function of preventing undesired particles inside the test section, improving the flow alignment and breaking the largest turbulent structures. Downstream of the honeycomb, the flow enters the settling chamber through three turbulence grids that are responsible for the abatement of turbulent flow fluctuations. Thanks to the major contration ratio, the flow is accelerated in the circular-to-square convergent up to the test section. The latter is mounted inside a room acoustically treated with 0.2 m of acoustic foam and an outer layer of plywood, in order to damp any type of disturbances, such as external background noise and reflections of the noise produced in the test section itself. Downstream of the test section, a main acoustic silencer is present to reduce sound propagation upstream from the the suction fan. Likewise of the test section acoustic room, the silencer is covered by a 0.2 m layer of acoustic foam and an outer layer of plywood. The axial fan, which is driven by a 9.9 kW variable-speed DC motor, is located at the end of the main silencer, and the air flows through a second silencer, that eventually lets the air out of the wind tunnel.

Usually, a wind tunnel design ensures that the flow at the inlet of the test section is with least possible turbulence intensity, i.e. with a regime as laminar as possible. However, since the interest of this work is to analyze a fully-developed turbulent boundary layer, then a set of 3 bands of sand paper is glued on the walls just at the end of the convergent, with a 0.001 m width and separated by 0.001 m. The tripping has the function of forcing boundary layer transition over a relatively short distance, leading to a fully-developed TBL along almost the entire test section.

There are three measurement stations inside the test section, as shown in Figure 3.2. By taking the side-length of the squared test section $l = 0.25\ m$ as reference, station 0, that corresponds to the inlet of the test section, is located at $0.6l$ downstream of the bands of sand paper. On the other hand, station 1 and 2 are located at $3.6l$ and $5.6l$ downstream of the tripping, respectively. At station 0, a thermocouple and a Pitot probe were used to get the inlet velocity U_∞, while hot-wire and microphone measurements have been performed at station 2.

Experiments are meant to be carried out at four different inlet velocities: 15, 20, 25 and 30 m/s. However, there will be a slight acceleration of the external velocity U_e along the wind tunnel due to the development of the boundary layer along the test section walls, that implies the presence of a fictional convergent. For this reason, external velocity in station 2 will be slightly different from inlet velocity.

3.2 Inlet velocity measurements

The measurement of the inlet velocity has been done by using a Pitot probe, placed in station 0 of the test section and aligned in streamwise direction. The Pitot probe is composed of two pressure taps: one placed in the stagnation point for the measure of

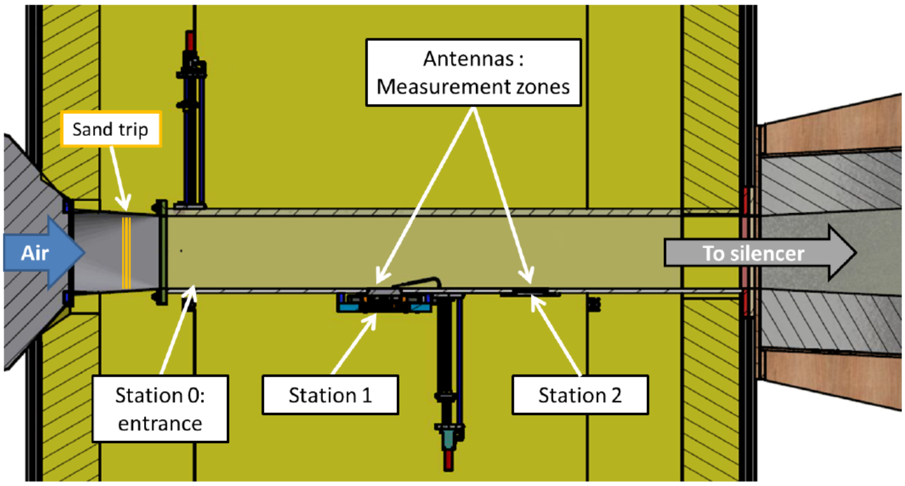

Figure 3.2: Measurement stations in the test section of the WAABLIEF facility [8].

total pressure p°, and one placed on the side wall of the probe for the measure of static pressure p_∞. The pressure difference $p^\circ - p_\infty$ is the dynamic pressure q_∞ and allows to evaluate the flow inlet velocity U_∞ by using Bernoulli's equation for an incompressible flow:

$$p^\circ - p_\infty = q_\infty = \frac{1}{2}\rho_\infty U_\infty^2 \tag{3.1}$$

Which leads to the expression for the inlet velocity:

$$U_\infty = \sqrt{\frac{2\,q_\infty}{\rho_\infty}} \tag{3.2}$$

In order to measure the dynamic pressure q_∞, the pressure taps of the Pitot probe are connected to a Valydine differential pressure transducer, that must be calibrated before using in order to convert the voltage output in terms of pressure measurement. Regarding the air density ρ_∞, it can be evaluated by using the ideal gas law:

$$\rho_\infty = \frac{p_\infty}{R\,T_\infty} \tag{3.3}$$

Where R = 287.05 J/(kg K) is the specific gas constant for air, and T_∞ is the air temperature measured in station 0 with a thermocouple.

3.2.1 Calibration of the pressure transducer

The pressure transducer is fundamental to obtain the dynamic pressure measured by the Pitot probe. The one used in the present work is a Validyne differential pressure transducer, which is composed by two pressure ports separated by a diaphragm. The latter is sensible to the pressure difference between the two ports, returning a voltage signal proportional to the pressure difference applied. Moreover, a model CD15

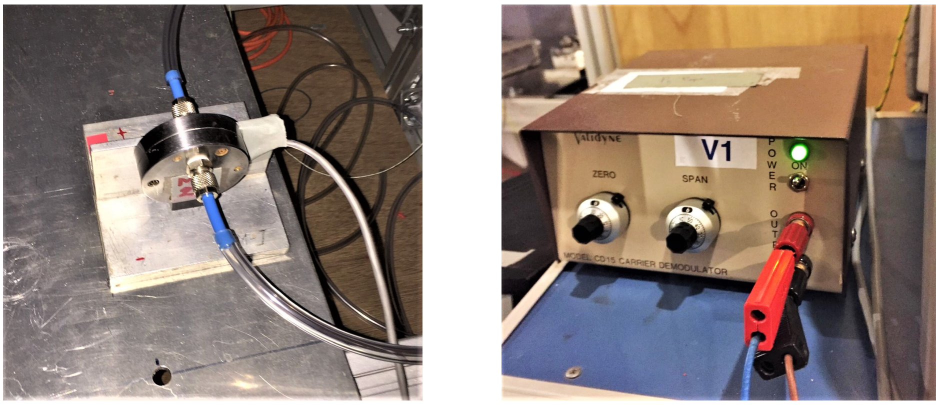

(a) Pressure transducer (b) Demodulator

Figure 3.3: Validyne differential pressure transducer (a) and model CD15 Validyne carrier demodulator (b).

Validyne carrier demodulator is connected to the pressure transducer for signal conditioning. The differential pressure transducer and the demodulator are illustrated in Figure 3.3.

Since the Validyne output is a voltage, a calibration procedure is needed to refer the signal in Volts to the corresponding pressure value in Pascals. The calibration curve is found by using a water manometer, composed by a water column in a tube whose ends are exposed to different pressures. The pressure difference Δp causes a difference of liquid height Δh in the tube, and these quantities are linked by Stevin's law:

$$\Delta p = \gamma_{wat}\,\Delta h \tag{3.4}$$

Where γ_{wat} is the specific weight of water. By knowing the height difference, that is readable from the manometer graduated scale, it is therefore possible to evaluate the corresponding pressure difference.

The calibration strategy for the pressure transducer is as follows:

- The first thing is the connection between the pressure transducer and the water manometer. The positive ends of the two devices are free to ambient pressure, while the negative ends are connected with each other through pneumatic tubes and linked to a syringe for the regulation of pressure difference. With this configuration, a positive pressure difference is generated by doing underpressure with the syringe.

- The voltage range regulation of the pressure transducer is done with the carrier demodulator. At first, the zero value without pressure difference must be set. The voltage span is adjusted afterwards, once reached the maximum pressure value of interest.

- Once the voltage range is set, several calibration points must be taken to obtain a precise calibration curve. For each point, the output voltage E coming from the pressure transducer and the corresponding height difference Δh in the manometer must be acquired. The pressure difference Δp can be matched with the output voltage by using Equation (3.4).

- Finally, all the calibration points can be fitted to find the calibration curve of the differential pressure transducer $\Delta p = f(E)$.

The calibration curve therefore allows to measure a pressure difference applied in the Validyne transducer by simply acquiring the corresponding output voltage. Once the relation is found, the differential pressure transducer is ready to be used with the Pitot probe for inlet velocity evaluation.

3.2.2 Inlet velocity measurement chain

For the measurement of inlet velocity, it is needed to compute air density ρ_∞ and dynamic pressure q_∞, according to Equation (3.2). For this reason, the thermocouple sensor and the Pitot probe must be mounted in station 0, as shown in Figure 3.4.

The probe is aligned in streamwise direction and connected to the calibrated Validyne differential pressure transducer through two pneumatic tubes, one for p° at the positive port and one for p_∞ at the negative port. With this connection, the output voltage of the transducer is indicative of the dynamic pressure q_∞ of the flow. The thermocouple sensor is simply connected to a temperature reader for the visualization of T_∞.

The pressure transducer is then connected to the demodulator, that sends the output voltage E to the National Instruments PXI for signal acquisition. The voltage acquired is therefore converted in dynamic pressure q_∞ by using the calibration curve $\Delta p = f(E)$. Regarding the air density ρ_∞, it can be easily computed by using Equation (3.3) with the value of T_∞ measured by the thermocouple sensor.

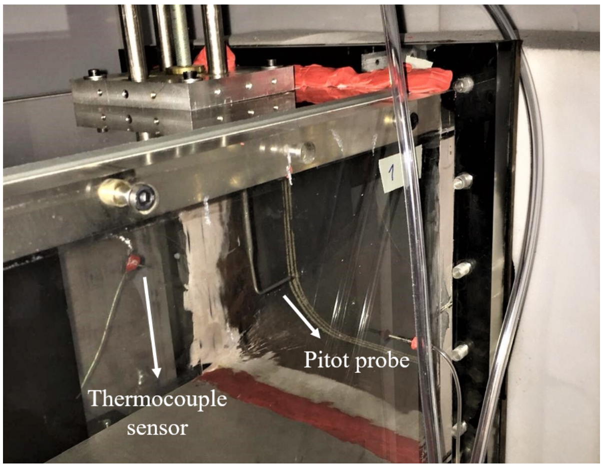

Figure 3.4: Pitot probe and thermocouple sensor mounted in station 0 of the test section.

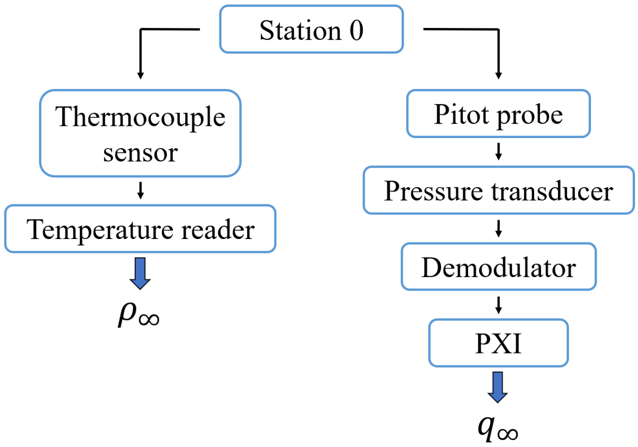

Figure 3.5: Schematic view of the inlet velocity measurement chain.

For each operating point of interest of the wind tunnel (which corresponds to a specific inlet velocity), dynamic pressure and air density are thus measured, and inlet velocity U_∞ can be finally computed by using Equation (3.2). A schematic view of the measurement chain is depicted in Figure 3.5.

3.3 Hot-wire measurements

Velocity measurements of the turbulent boundary layer over the flat plate in station 2 of the test section were performed by using a hot-wire anemometry system with a single-sensor probe at constant temperature. For this type of system, the hot-wire temperature is maintained constant by the control circuit shown in Figure 3.6. The wire is cooled by the flow velocity leading to a change of resistance, which in turn causes an unbalance in the Wheatstone bridge of which the wire is connected to. In order to maintain a constant temperature in the wire, the control circuit amplifies the output voltage coming from the bridge, in order to control the supply voltage required to maintain the wire temperature constant [15]. As a consequence, the amplifier output voltage E turns out to be a function of the flow velocity U.

The hot-wire anemometry is one of the most used and successful velocity measurement techniques for turbulent flows. The main advantage of this technique is the high frequency response, which can reach even 100 kHz. As the highest frequencies in air flows have values around 10 kHz, the frequency response of the hot-wire technique is perfect to characterize the velocity fluctuations in the entire frequency range. Moreover, it has a good spatial resolution because of the small size of the sensor.

Conversely, the main drawback is related to the punctiform measurement, which results in an impossibility to measure the velocity field in different points of the space simultaneously with a single probe. Moreover, this technique represents an intrusive method for the flow, as the hot-wire probe is directly introduced into the flow.

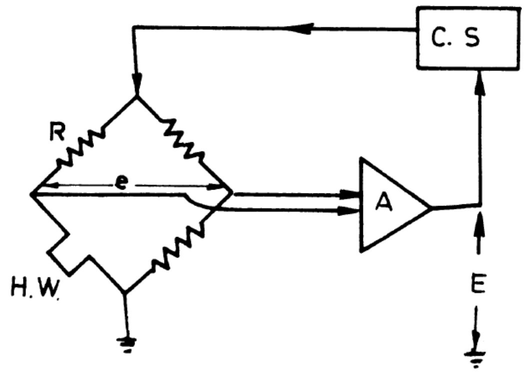

Figure 3.6: Schematic view of the constant temperature control circuit [15].

3.3.1 Hot-wire calibration

As the output coming from a hot-wire anemometry system is a voltage, the hot-wire technique needs a calibration in order to refer the signal in Volts to the corresponding velocity value in m/s. In order to perform the calibration, a flow with known velocity characteristics is necessary.

In the present work, a jet flow coming out of a pressurized nozzle has been used for the calibration. The nozzle is shown in Figure 3.7: the device is connected to the pressure line in order to create a pressure difference between the settling chamber of the nozzle and the ambient pressure at the outlet, which leads to a jet flow coming out of the nozzle. The jet flow represents a good choice for hot-wire calibration, as the velocity field is well-known. Indeed, in the potential core the velocity is uniform and constant, equal to the value at the jet outlet. As the potential core is extended up to distances from the outlet around 3 or 4 times the exit cross-section diameter, the hot-wire sensor must be close to the jet outlet and centered in the axial direction of the flow.

The strategy to compute the jet velocity in the potential core exploits the conservation of mass flow and total pressure along the nozzle. For a steady, incompressible flow, the conservation of mass flow between the settling chamber and the outlet of the nozzle can be written as:

$$A_{sc}\,U_{sc} = A_{out}\,U_{out} \tag{3.5}$$

Where U_{sc} and U_{out} are the flow velocity in the settling chamber and at the outlet, while A_{sc} and A_{out} are the settling chamber and outlet cross-sectional area, respectively. Since the nozzle contraction is high, A_{sc} is much larger than A_{out}, namely $A_{sc} \gg A_{out}$. Considering this relation, Equation (3.5) leads therefore to the approximation $U_{sc} \ll U_{out}$.

Assuming zero total pressure loss in the nozzle, the following relation can be written by using Bernoulli's equation (3.1):

$$p_{sc} + \frac{1}{2}\rho_{sc}U_{sc}^2 = p_{out} + \frac{1}{2}\rho_{out}U_{out}^2 \tag{3.6}$$

Figure 3.7: Pressurized nozzle used for hot-wire calibration.

As $U_{sc} \ll U_{out}$, the dynamic pressure in the settling chamber is negligible and Equation (3.6) can be approximated as:

$$p_{sc} \approx p_{out} + \frac{1}{2}\rho_{out}U_{out}^2 \tag{3.7}$$

The static pressure in the settling chamber p_{sc} can be therefore considered as an indication of the flow total pressure. It is thus possible to estimate the potential core velocity by measuring the static pressure difference between settling chamber and jet outlet:

$$U_{out} \approx \sqrt{\frac{2\,(p_{sc} - p_{out})}{\rho_{out}}} \tag{3.8}$$

The static pressure difference can be measured by connecting the settling chamber pressure tap of the nozzle to the positive port of the Validyne pressure transducer and leaving the negative port to ambient pressure, which is also the outlet static pressure. The flow density is computed by measuring the temperature with the thermocouple and by using Equation (3.3). Once the flow velocity in the potential core is known, the hot-wire calibration can be performed.

Two types of hot-wire calibrations are needed to perform flow measurements with the hot-wire technique:

1. The dynamic calibration is intended to regulate and improve the frequency response of the sensor. The final aim is to find an optimal frequency response and the corresponding limiting frequency of the system.

2. The static calibration is necessary to find the relation between the output voltage E and the corresponding flow velocity U. With the calibration curve, it is possible to retrieve the flow velocity by acquiring the voltage signal coming from the hot-wire system.

A detailed explanation of the two calibration procedures is given below.

Hot-wire dynamic calibration

The hot-wire system is characterized by a frequency response that is dependent upon the control circuit configuration and the thermal inertia of the sensor. In order to have an optimal regulation, the dynamic calibration must be performed.

The hot-wire sensor is connected through a cable to the anemometer that contains the Wheatstone bridge regulated by the constant temperature control circuit. The anemometer allows to adjust the compensation inductance of the Wheatstone bridge and the amplifier offset voltage, in order to achieve an optimal regulation and have a maximally flat frequency response.

The usual approach to evaluate the result of this regulation is by performing the square-wave test: a square-wave current generated by the anemometer is injected at the wire terminal, leading to a response of the system that can be monitored by using an oscilloscope connected to the anemometer. Theoretically, the square-wave current is a pulse signal, but the real frequency response of the hot-wire system leads to a wave form that tends to the square wave, as shown in Figure 3.8. The characteristic response-time τ_c of the given configuration is then evaluated by taking the interval in which the 36.8% of the maximum peak reached by the wave is found, as illustrated in Figure 3.8 [15]. Finally, the limiting frequency is computed by using the following definition:

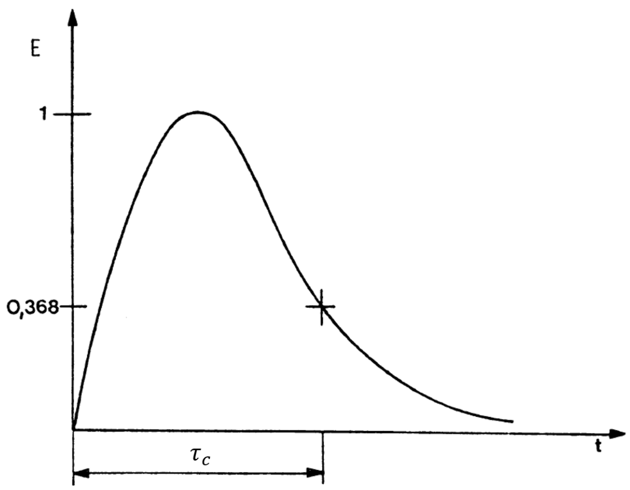

Figure 3.8: Typical wave form of the real frequency response of the hot-wire after a square-wave current test [15].

$$f_{max} = \frac{1}{2.02\,\tau_c} \tag{3.9}$$

As the frequency response depends on flow conditions, the dynamic calibration must be performed with the most critical flow of interest, i.e. the highest flow velocity considered in the experimental campaign. For this reason, the dynamic calibration has been performed with a jet velocity equal to 30 m/s, which is the maximum velocity of interest for the present work. Once the circuit regulation has been done, the resulting dynamic response for this velocity is shown on the oscilloscope in Figure 3.9. The estimated response-time for this case is $\tau_c = 50\,\mu$s, which leads to a maximum frequency response of $f_{max} \approx 9.9$ kHz.

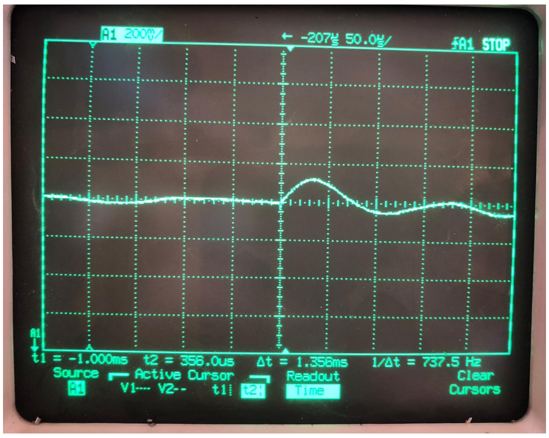

Figure 3.9: Oscilloscope displaying the frequency response of the hot-wire system during a square-wave test.

Once the limiting frequency is finally obtained, a cut-off frequency equal to f_{max} must be set on the anemometer amplifier in order to filter the output signal from frequencies above the maximum frequency response. As the filtering frequency has discrete levels, its value cannot be set to exactly 9.9 kHz, therefore a cut-off frequency of 10 kHz has been chosen.

Hot-wire static calibration

Once the filtering frequency is set on the anemometer amplifier, the static calibration can be performed. The procedure consists of characterizing the entire velocity range of interest with several velocity points, which correspond to different hot-wire voltages.

In order to relate the jet velocity with the corresponding hot-wire voltage, the pressure tap of the nozzle settling chamber is connected to the calibrated Validyne pressure transducer, and the Validyne signal is acquired simultaneously to the hot-wire signal. For the acquisition, the pressure transducer is connected to its demodulator as already explained in Subsection 3.2.2, while the anemometer must be connected to the amplifier with the chosen filtering frequency as shown in Figure 3.10. The

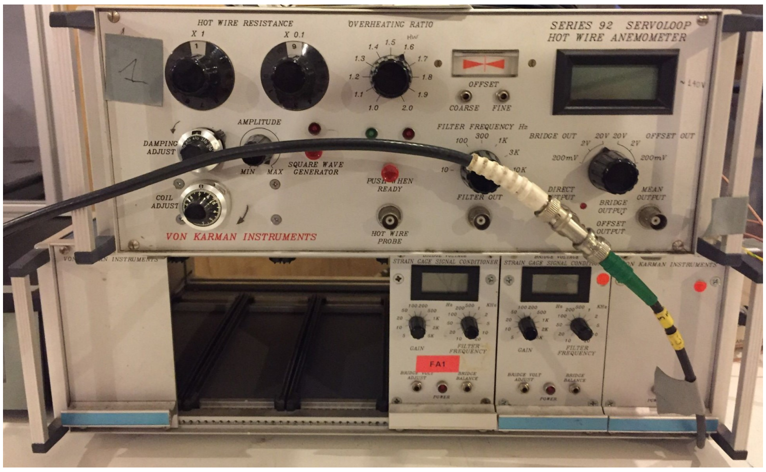

Figure 3.10: Hot-wire anemometer cointaining a constant temperature control circuit, and its amplifier that allows the choice of filtering frequency and gain.

Validyne demodulator and anemometer amplifier are then connected to PXI for signal acquisition.

Once the calibration points have been acquired, the hot-wire calibration curve $U = f(E)$ is founded by fitting the calibration points. As the relation between velocity and voltage depends on the relation for the heat transfer from a body immersed in a flow field, the calibration curve is non-linear and with a maximum sensitivity at low velocities [15]. A typical hot-wire calibration curve is depicted in Figure 3.11. As a consequence of this behaviour, more calibration points must be acquired for lower velocities in order to properly characterize the low-velocity range.

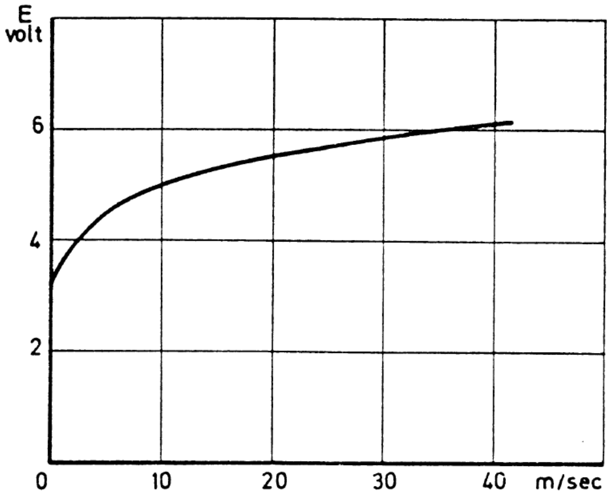

Figure 3.11: Typical non-linear calibration curve of a hot-wire system [15].

Another problem of the static calibration is the dependence upon the ambient temperature. Indeed, slight temperature changes during the days heavily affect the hot-wire signal and therefore a daily static calibration is needed for the hot-wire sensor.

3.3.2 Hot-wire measurement chain

Once the dynamic and static calibration are completed, the hot-wire measurements for the characterization of the velocity profiles over the flat plate in wind tunnel can be finally performed.

The hot-wire probe is mounted on an automated movement system that allows the sensor positioning in streamwise and wall-normal direction through an electric motor. The latter is managed by a particular LabView software that enables the choice of streamwise and wall-normal positions of interest. Once the positions are set on the software, the movement system is capable of acquiring automatically the hot-wire signal in every position of interest. The automated movement system and an example of hot-wire positioning over the 64-microphone antenna are shown in Figure 3.12.

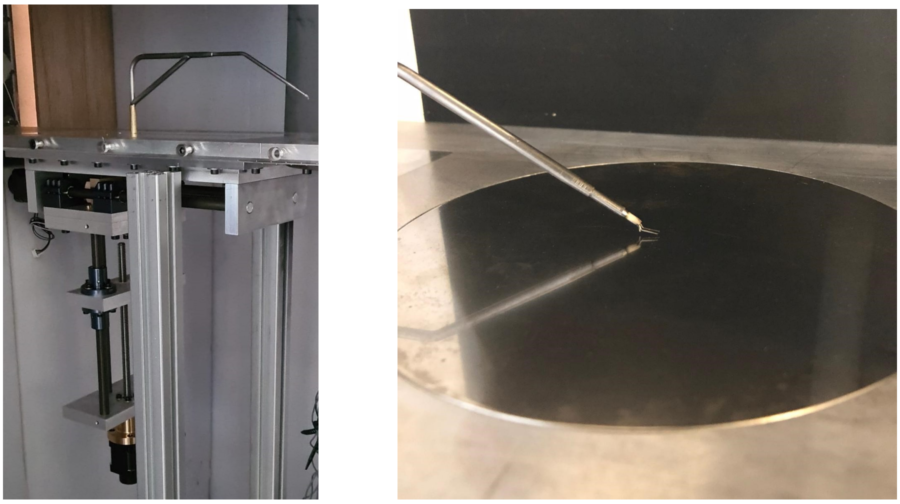

(a) Movement system (b) Hot-wire probe in position

Figure 3.12: Hot-wire automated movement system mounted downstream of station 2 (a) and an example of hot-wire positioning for TBL velocity measurements over the antenna (b).

In order to properly measure the TBL velocity profile over the flat plate, several points in wall-normal direction must be considered. As velocity gradients are greater while the distance from the wall decreases, more points must be considered in the vicinity of the wall in order to have a good characterization of the turbulent profile. Once the hot-wire signal for every position of interest is acquired, the velocity profile is finally retrieved by using the calibration curve $U = f(E)$.

3.4 Wall-pressure measurements

The measurements of unsteady wall-pressure fluctuations beneath the TBL were performed in station 2 of the test section by using a 64-microphone antenna that has been designed at VKI by Schram and Van de Wyer [22].

The microphone array is installed in a circular steel plate with a diameter of 0.186 m, of which upper surface can be flush-mounted with the bottom wall of the test section. Within a 0.15 m-diameter usable disk area, 64 electret microphones (Knowles model FG-23329-C07) are mounted by following an optimized positioning pattern. The electrets have a small size with a 0.0026 m-diameter of the sensing head, and provide a relatively flat frequency response up to 10 kHz. The microphones are not flush-mounted with the upper surface, but instead face the grazing flow through a 0.5 mm-diameter pinhole in order to increase spatial resolution. A schematic view of antenna and line-cavity arrangement is shown in Figure 3.13.

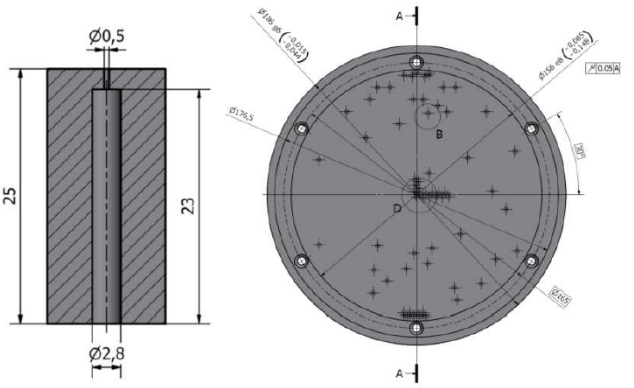

Figure 3.13: CAD drawing of antenna (on the right) and line-cavity arrangement (on the left). The electret is placed at the end of the 2.8 mm-diameter cavity and connected to the grazing flow through the 0.5 mm-diameter pinhole [22].

In the present work, only the L-shaped microphone array located in the center of the antenna has been used. The array contains 16 microphones spaced in a L-shaped pattern with 2 mm of spacing in between. For the measurements, the long edge of the array has been aligned with streamwise direction x, and consequently the short edge with spanwise direction z. Microphone positioning and numbering in the array are illustrated in Figure 3.14.

3.4.1 Calibration of electret microphones

If on the one hand the pinhole arrangement offers an advantage in terms of spatial resolution, on the other it alters the dynamic response of the microphone. For this reason, a calibration procedure for the electret microphones is required to correct for the amplitude modulation and phase lag of the line-cavity system [22].

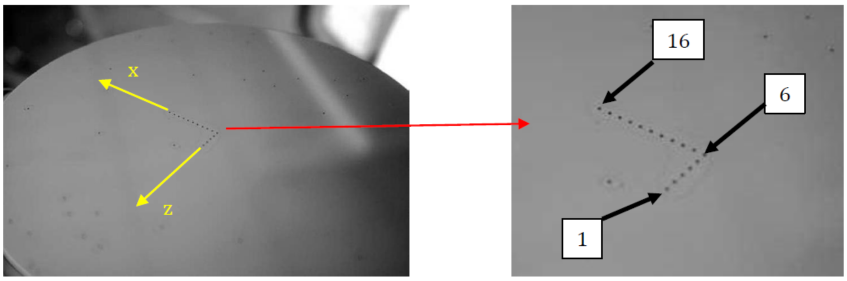

Figure 3.14: L-shaped microphone array of the 64-microphone antenna. Measurement positioning (on the left) and microphone numbering (on the right) are highlighted in the pictures [3] (original source [22]).

The general idea is to refer the electret microphone to a Brüel & Kjær (B&K) model 4938 1/4-inch microphone, which is of better quality and much more expensive than the electret. The B&K reference microphone is flush-mounted on an auxiliary flat plate. In order to perform the calibration, a calibrator device is needed to provide an intermediate signal for a two-step calibration procedure. The device consists of a steel cylinder drilled in the middle to accomodate a 0.013 m-diameter channel that guides the acoustic waves emitted by a loudspeaker towards the end of the duct, where the microphone to calibrate is placed. The diameter of the channel is large enough to ensure plane wave propagation up to 15.152 kHz. Moreover, a side-branch channel is present to accomodate a calibrator B&K microphone (same model as the reference microphone) that represents the intermediate signal of the calibration. A representation of the calibrator device is given in Figure 3.15.

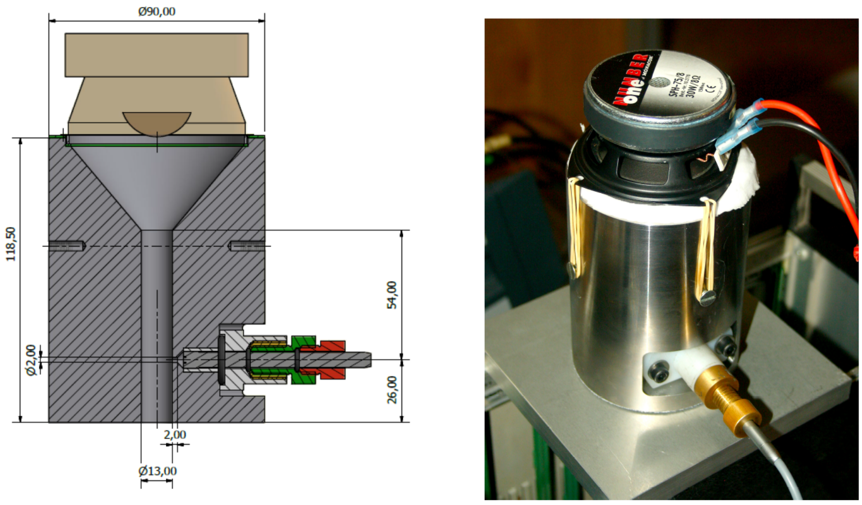

Figure 3.15: CAD drawing (on the left) and picture (on the right) of the calibrator device with the loudspeaker above [2].

The aim of the calibration is to find the Transfer Function (TF) between the reference and electret microphone, i.e. the function by which the electret signal should be multiplied to yield the pressure level that would have been measured by the reference B&K in the same conditions of the electret microphone. The result is a calibrated signal that contains the information of the reference microphone, although is acquired by a much cheaper electret microphone. As the reference microphone is flush-mounted, the alteration of the dynamic response is avoided while maintaining the advantage in spatial resolution given by the pinhole arrangement.

Two different types of calibration are needed to compute the proper TF:

1. A static calibration is necessary to find the sensitivity of the B&K microphones. This parameter is important because it allows the right signal conversion from Volts to Pascals, which is fundamental to know the exact pressure level to which the microphones are exposed.

2. The dynamic calibration is intended to find the final TF in frequency domain between the reference and electret microphone through a two-step procedure. The calibrator device is the key element of this process.

A detailed explanation of the two calibration procedures is given below.

Static calibration of B&K microphones

Static calibration has been performed by using a type 4231 B&K Pistonphone that generates a 94 dB acoustic field with a 1 kHz wave. The microphones are connected to a type 2692-C B&K NEXUS Conditioning Amplifier, which has the task of signal conditioning. These two devices are illustrated in Figure 3.16.

(a) Pistonphone (b) NEXUS Amplifier

Figure 3.16: B&K Pistonphone [25] (a) and B&K NEXUS Conditioning Amplifier (b) used for static calibration of B&K microphones.

The calibration procedure starts with the setting of a trial sensitivity on the amplifier and the positioning of the microphone to calibrate inside the pistonphone. Then a signal acquisition is made while generating the known acoustic field of 94 dB. By comparing the SPL computed with the time-series acquired and the known SPL of 94 dB, it is possible to obtain a correction factor useful to get the real sensitivity of the microphone.

Once the right sensitivities are retrieved, the values must be set on NEXUS Amplifier in order to have the a gain that leads to the right signal conversion from Volts to Pascals. In the present work, a value of 1.49 and 1.41 mV/Pa have been obtained for calibrator and reference microphone, respectively.

Microphones dynamic calibration

Once the static calibration of B&K microphones is done, the following task is to perform the dynamic calibration. To do this, a signal generator is needed to generate an acoustic field through the loudspeaker into the calibrator device. For this purpose, a type 33120A Agilent Arbitrary Waveform Generator has been used and connected to a model 6230 JBL Power Amplifier, which amplifies the input signal and sends it to the loudspeaker. Agilent signal is also sent to the National Instruments PXI for its acquisition.

The dynamic calibration obviously requires the calibrator and reference B&K microphones and the electret microphones placed in the L-shaped array of the antenna. The first are connected to NEXUS Amplifier, while the second are plugged into a proper amplifier for electret microphones designed at VKI. The latter allows to choose between three different gains for signal conditioning: 1, 10 and 100. The two amplifiers are then connected to PXI for signal acquisition. A schematic view of the whole dynamic calibration chain is shown in Figure 3.17.

Once the input signal coming from Agilent is chosen, the calibration procedure can start. Dynamic calibration is performed in two steps, as shown in Figure 3.18:

1. In Step 1, the calibrator device is placed on top of the auxiliary flat plate, with the central channel aligned with the reference B&K microphone. The sound emitted by the loudspeaker propagates through the central duct to the openings located at the bottom and side, where reference and calibrator B&K microphones are placed, respectively. The signals acquired by the two microphones provides the first frequency-dependent transfer function:

$$TF_1 = \frac{\mathcal{F}(p'_{ref})}{\mathcal{F}(p'_{cal})} \tag{3.10}$$

   That represents the TF between reference and calibrator microphone.

2. In Step 2, the calibrator device is placed on top of the 64-microphone antenna, with the central channel aligned with the electret of the L-shaped microphone array to calibrate. This time the sound propagates to the electret passing through the pinhole. The transfer function of this step therefore includes the effect of the

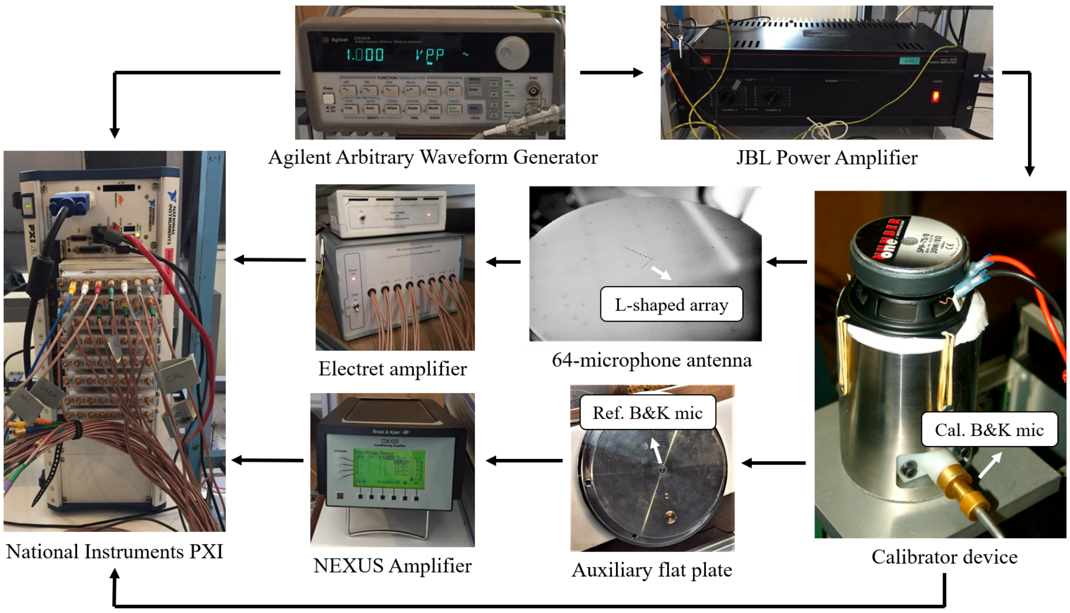

Figure 3.17: Schematic view of dynamic calibration chain for the microphones.

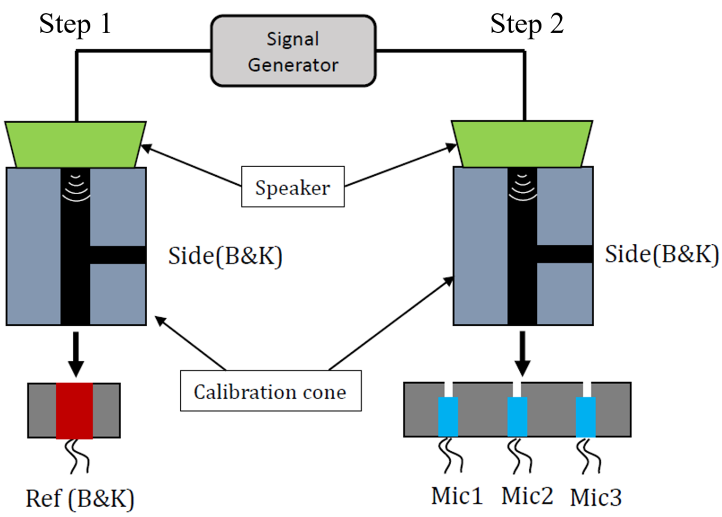

Figure 3.18: Schematic representation of the dynamic calibration procedure [3].

line-cavity system in which the electret microphone is placed:

$$TF_2 = \frac{\mathcal{F}(p'_{cal})}{\mathcal{F}(p'_{ele})} \tag{3.11}$$

That represents the TF between calibrator and electret microphone.

Since the calibrator microphone is used as intermediate signal, the final transfer function between reference and electret microphone can be obtained by multiplying Equation (3.10) and (3.11):

$$TF = TF_1 \cdot TF_2 = \frac{\mathcal{F}(p'_{ref})}{\mathcal{F}(p'_{cal})}\frac{\mathcal{F}(p'_{cal})}{\mathcal{F}(p'_{ele})} = \frac{\mathcal{F}(p'_{ref})}{\mathcal{F}(p'_{ele})} \tag{3.12}$$

With the assumption that the acoustic field in the calibrator side-channel is the same when calibrating the reference or electret microphone. By converting B&K signals in Pascals, the final TF turns out to be a [Pa/V] unit, therefore it contains also the information for signal conversion. Thus, by simply multiplying it for the electret signal acquired in test section of the wind tunnel, the pressure level in Pascals that would have been measured by the reference B&K is retrieved.

3.4.2 Wall-pressure measurement chain

During the wind-tunnel experiments, the steel circular antenna is flush-mounted in station 2 with the bottom wall of the test section. The L-shaped microphone array is oriented as already shown in Figure 3.14. Although the development of the boundary layer along the test section walls implies a slight flow acceleration, the present case can be considered as a ZPG configuration.

The 16 electret microphones are plugged into the amplifier, which in turn is connected to PXI for signal acquisition. The signal in the PXI is filtered and converted from analog to digital environment, and then acquired by the acquisition system and transferred to the user interface for signal visualization. A schematic view of the measurement chain is depicted in Figure 3.19.

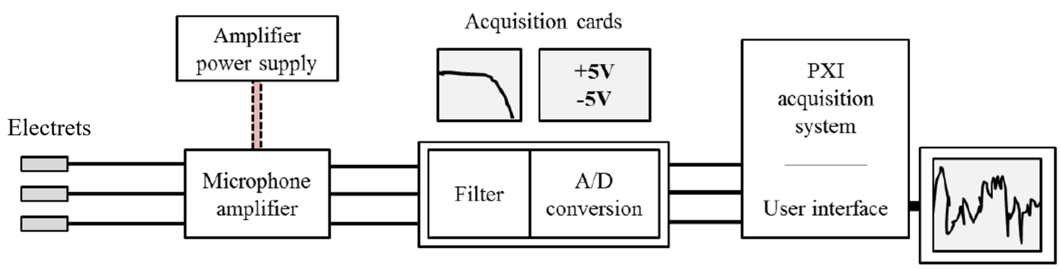

Figure 3.19: Schematic view of the wall-pressure measurement chain [8].

For each operating point of interest of the wind tunnel, wall-pressure measurements using the L-shaped array are performed, simultaneously to inlet velocity measurements already explained in Subsection 3.2.2. By using the final TF obtained from the calibration, PSD and cross-coherence of wall-pressure fluctuations within the TBL are therefore computed. The comparison between TBL statistical models for ZPG case and experimental results can be finally achieved.

Chapter 4

Results for velocity measurements

4.1 Inlet velocity results

In this Section, the results from the calibration of the Validyne differential pressure transducer and the Pitot probe measurements are presented. Moreover, an alternative strategy to measure the inlet velocity is introduced and compared to the classical procedure with the Pitot probe, in order to see its feasibility.

4.1.1 Results of Pitot probe measurements

As already explained in Section 3.2, a calibration of the Validyne differential pressure transducer is needed to use the Pitot probe for the inlet velocity measurements in station 0. The pressure transducer has been calibrated within a pressure range between 0 and 80 mm of water height, which is enough for the velocities of interest of the present case. The voltage range has been set to have a span between -5 and 5 V. To reconstruct the calibration curve $\Delta p = f(E)$, 17 different points of the pressure scale have been acquired, and the result is shown in Figure 4.1. The behaviour of the Validyne transducer turns out to be linear, as it is expected from a regular differential pressure transducer.

Once the calibration curve is obtained, the inlet velocity U_∞ can be easily measured by using the Pitot probe and the thermocouple mounted in station 0. Dynamic pressure and temperature measurements have been acquired simultaneously to wall-pressure measurements with the antenna, and the inlet velocities are computed in the post-processing using Equation (3.2) and (3.3).

Four different operating points of the axial fan of WAABLIEF facility are considered in the present case, which correspond to four different inlet velocities. The results are shown in Table 4.1. The inlet velocities of the four cases considered span between approximately 15 and 30 m/s, which represents a fairly extensive range to see the effect of Reynolds number on flow parameters.

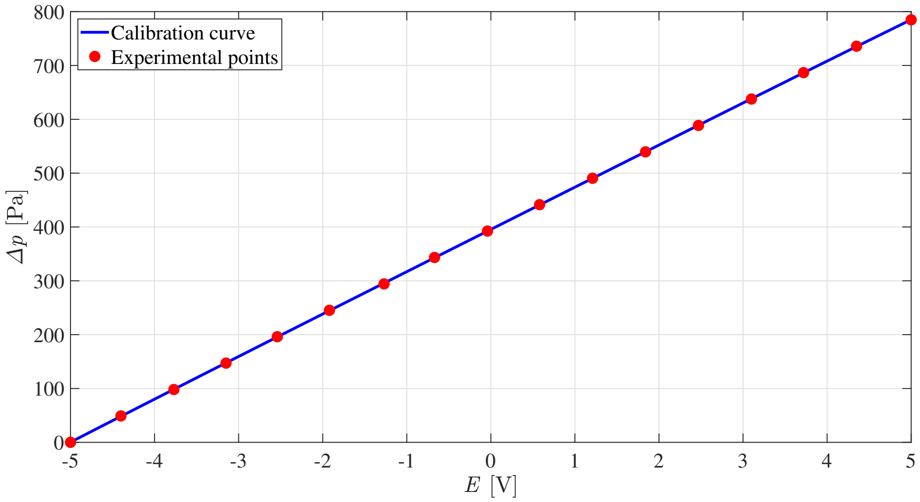

Figure 4.1: Calibration curve $\Delta p = f(E)$ of the Validyne differential pressure transducer.

f_{fan} [Hz]	U_∞ [m/s]
8	15.069
10.5	19.769
13	24.621
16	30.412

Table 4.1: Four operating points considered at different frequencies of the axial fan of WAABLIEF facility, and the corresponding four different inlet velocities.

4.1.2 Alternative measurement strategy for inlet velocity

During the experimental campaign, an alternative method to compute the inlet velocity has been studied. The aim of this analysis is to see the possibility of removing the Pitot probe from the inlet velocity measurement chain, as it represents an intrusive measuring instrument for the flow.

The alternative strategy exploits the same strategy adopted for the computation of the jet velocity out of the nozzle, already explained in Subsection 3.3.1. As the convergent contraction is very high, the static pressure in the settling chamber p_{sc} of the wind tunnel can be therefore considered as an indication of the flow total pressure. It is thus possible to estimate the inlet velocity by measuring the static pressure difference between settling chamber and inlet of the test section:

$$U_\infty \approx \sqrt{\frac{2\,(p_{sc} - p_\infty)}{\rho_\infty}} \tag{4.1}$$

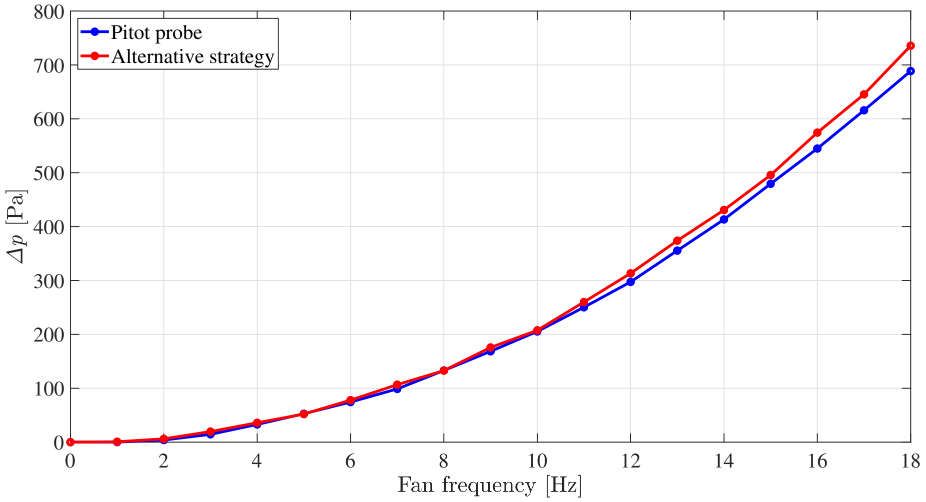

Figure 4.2: Dynamic pressure measured with the Pitot probe in station 0 compared with the static pressure difference between settling chamber and inlet of the test section.

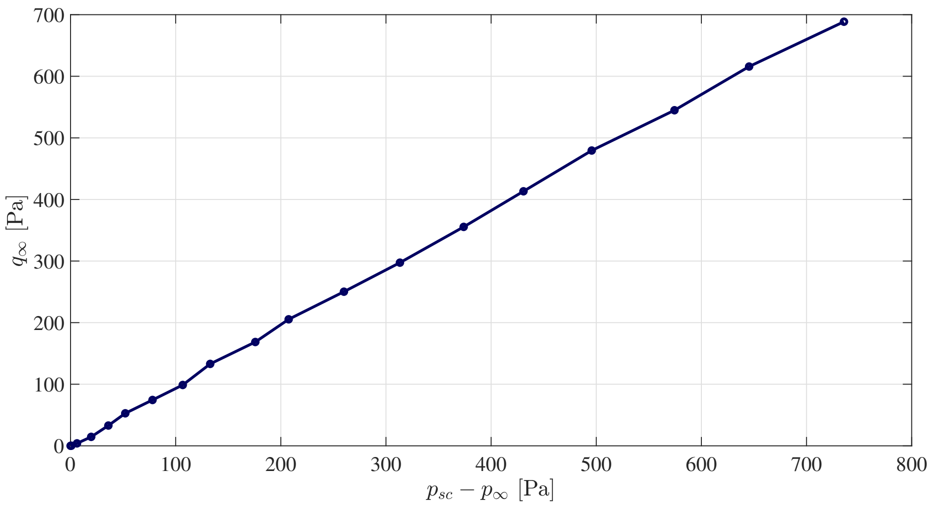

Figure 4.3: Calibration curve $q_\infty = f(p_{sc} - p_\infty)$ that relates the dynamic pressure measured with the Pitot probe with the static pressure difference between settling chamber and inlet of the test section.

The static pressure difference can be measured by connecting a settling chamber pressure tap to the positive port of the Valydine pressure transducer and a inlet pressure tap to the negative port. The result of this alternative procedure is shown in Figure 4.2 for several operating points and compared with the actual dynamic pressure measured by the Pitot probe in station 0.

The agreement between the static pressure difference $p_{sc} - p_\infty$ and the real dynamic pressure q_∞ turns out to be fairly good. However, a discrepancy between the two curves can be noted at higher fan frequencies, which means that an error in the computation of inlet velocity with the alternative method occurs at higher velocities. Moreover, the error quadratically enhances as the velocity increases: this is probably due to a small total pressure loss along the convergent, which is a quadratic function of the flow velocity.

One way to avoid the discrepancy is to find a calibration curve $q_\infty = f(p_{sc} - p_\infty)$ that allows to compute the actual dynamic pressure q_∞ by measuring the static pressure difference $p_{sc} - p_\infty$. The calibration curve is illustrated in Figure 4.3.

In conclusion, the alternative method proves to be a valid procedure for inlet velocity measurement, but less precise than the Pitot probe. For this reason, the Pitot probe has been chosen to perform inlet velocity measurements in the present work. Indeed, the intrusiveness of the instrument is minimal and negligible for the present case, therefore measurement precision was preferred.

4.2 Hot-wire results

In this Section, the results from the hot-wire static calibration are shown and explained. Then, the TBL velocity profiles are presented and compared with the models available in literature, and the TBL parameters needed for WPS normalization are computed.

4.2.1 Static calibration results

As already explained in Section 3.3, a static calibration of the hot-wire sensor is needed to know the relation between output voltage and flow velocity. The hot-wire has been calibrated within a jet velocity range between 0 and 30 m/s, which contains the velocities of interest of the present work. To reconstruct the calibration curve $U = f(E)$, 10 different points of the velocity scale has been acquired with a sampling frequency of $f_s = 51.2$ kHz and an acquisition time of $t_s = 10$ s. The very high value of f_s ensures that Nyquist's rule $f_s \geq 2\, f_{max}$ is respected, and therefore signal aliasing is avoided. The calibration points has been chosen to have more points at low velocity, in order to define properly the low-velocity range as already explained in Subsection 3.3.1.

During the calibration, the hot-wire probe has been calibrated with the jet flow in binormal direction, as shown in Figure 4.4a. As the effective cooling velocity depends on flow direction, this effect must be considered during the computation of the calibration curve. Indeed, the formulation for the effective cooling velocity can be expressed by Jorgensen relation [15]:

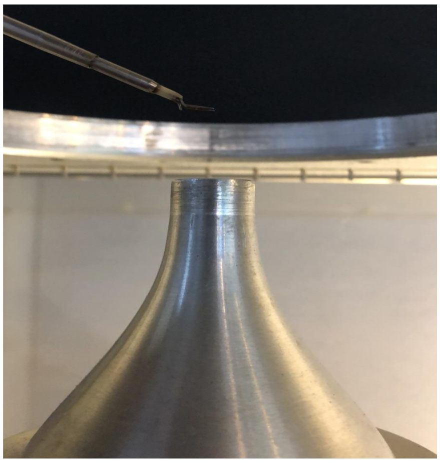

(a) Calibration positioning

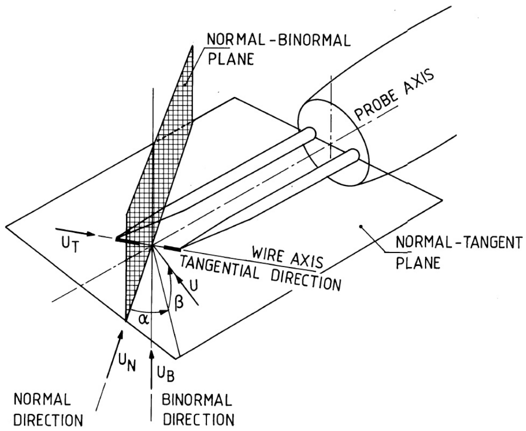

(b) Directions definition

Figure 4.4: Hot-wire positioning during static calibration (a) and the definitions of the three velocity directions for a hot-wire sensor (b) [15].

$$U_{eff}^2 = U_N^2 + k_T^2\, U_T^2 + k_B^2\, U_B^2 \tag{4.2}$$

Where subscripts N, T and B are referred to normal, tangential and binormal direction defined in Figure 4.4b, respectively. The coefficients k_T and k_B include the cooling effects of the tangential and binormal velocity components, respectively. Since during the calibration the jet flow is mostly in binormal direction, the velocity components U_N and U_T are negligible and the cooling velocity for the present case can be written as:

$$U_{eff}^2 = k_B^2\, U_B^2 \tag{4.3}$$

The coefficient k_B is a parameter that accounts for the acceleration of the flow over the wire located between the two prongs, and is typically around 1 to 1.1. Its value must be found experimentally through an angular calibration because it is dependent on the specific hot-wire probe used. As the angular calibration is missing in the present work, the k_B value has been assumed as 1.05. However, this assumption is a temporary solution to take into account the binormal effect in the present work, but further investigations must be done to find a proper solution for the static calibration procedure.

By correcting with k_B the jet velocity measured using the Validyne in order to get the real cooling velocity U_{eff}, the calibration curve $U_{eff} = f(E)$ can be finally obtained by matching the cooling velocity with the corresponding hot-wire output voltage. The result of the static calibration is shown in Figure 4.5: the non-linear calibration curve, fitted with a 4^{th} order polynomial law, proves to be in agreement with the typical static response already explained in Figure 3.11.

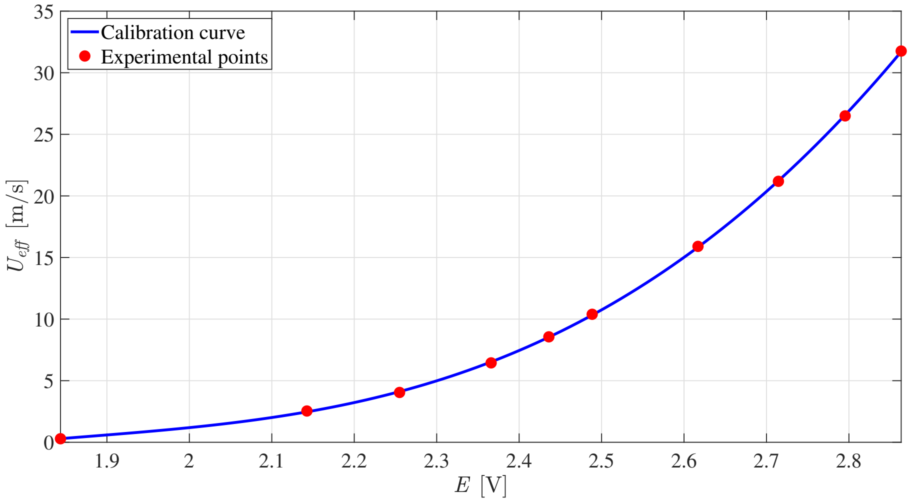

Figure 4.5: Calibration curve $U_{eff} = f(E)$ of the hot-wire sensor.

4.2.2 Wind tunnel results

Once the static calibration is completed, the velocity measurements in the wind tunnel can be performed to characterize the boundary layer over the antenna.

For the acquisition, 14 different points have been chosen in wall-normal direction, with the strategy to have more points near the wall as it is the region with the highest velocity gradients. The closest point to the wall has been set at 1 mm from the surface. This choice has been made to avoid wire breakage: indeed, the automated system has a few oscillations when positioning the probe, and a contact with the wall may lead to a sensor breakage, as the hot-wire is very fragile. Regarding the streamwise positions, 6 different stations have been chosen, corresponding to the positions of electrets number 6, 7, 8, 10, 13 and 16. By taking electret number 6 as reference system origin, the x-positions are 0, 2, 4, 8, 14 and 20 mm, respectively. The reason of this choice is due to an experimental strategy that will be explained later in Subsection 5.2.1.

As hot-wire measurements and wall-pressure measurements are performed separately, the flow conditions must be checked in order to have the same flow for both measurements. For this reason, a check-up of the inlet velocity in station 0 has been done before starting the hot-wire measurements, in order to match the same values shown in Table 4.1. A problem has been evidenced during this procedure: with the same fan frequencies of Table 4.1, the inlet velocities are much lower with the hot-wire system mounted in the wind tunnel. This is probably due to the blockage of the hot-wire system that influences the pressure difference between the air intake and the axial fan section. Another reason may be a total pressure loss in correspondence of the hot-wire support: indeed, the hot-wire probe is moved passing through an aperture downstream of station 2 that could create leakage. In order to avoid the discrepancy of inlet velocities, the fan frequencies has been enhanced and regulated in order to have the same U_∞ of Table 4.1 during the hot-wire campaign.

After this problem has been solved, the final velocity measurements have been performed for the four inlet velocities of interest. For the acquisition, a sampling frequency of $f_s = 51.2$ kHz and an acquisition time of $t_s = 10$ s have been set for each point. During the post-processing, the TBL parameters have been obtained by using the definitions presented in Chapter 2, and therefore velocity profiles can be retrieved.

According to Van de Wyer et al. [2], the velocity profile in a fully turbulent boundary layer over a smooth flat plate for an incompressible flow can be approximated by using the $1/7^{th}$ power law:

$$\frac{\bar{U}}{U_e} = \left(\frac{y}{\delta}\right)^{1/7} \tag{4.4}$$

The experimental mean velocity profiles compared to the power law are shown in Figure 4.6 for the particular streamwise position of $x = 0$ mm. The experimental curves prove to be in fair agreement with the theoretical $1/7^{th}$ power law, especially for the case of higher velocities. This is an indication that the boundary layer over the antenna in station 2 is fully turbulent as expected.

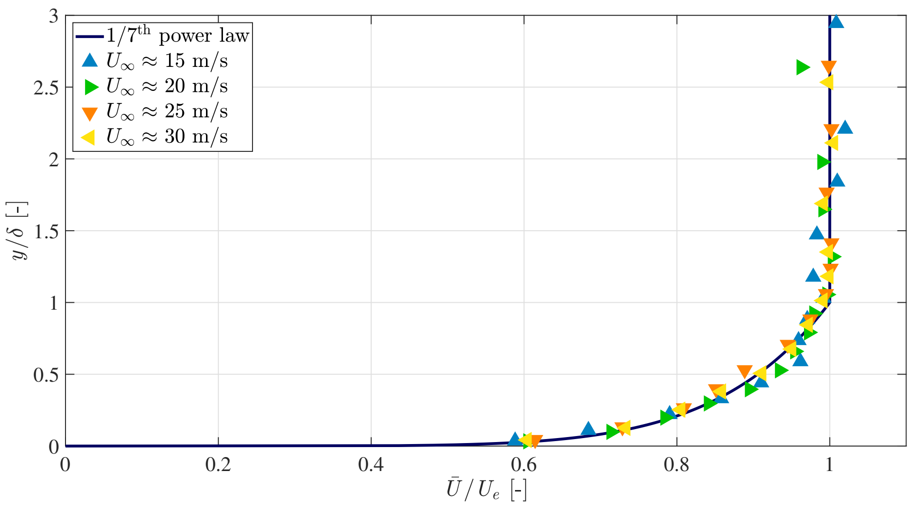

Figure 4.6: Mean velocity profiles over the antenna in station 2 for the different operating points of interest at $x = 0$ mm, compared with the $1/7^{th}$ power law.

It is also interesting to compute the velocity profiles in wall variables y^+ and U^+ defined in Equation (2.16) and (2.17), in order to identify the various regions of the TBL structure and compare the results with the universal Law of the Wall proposed by Spalding in Equation (2.21). For the skin friction coefficient c_f, the Bradshaw's method has been used. This method is based on the observation that the point at $y^+ = 100$ corresponds to a value of $u^+ = 16.24$, leading to this expression [10]:

$$u^+ y^+ = 1624 = \frac{\bar{U}}{u_\tau}\frac{y\,u_\tau}{\nu} = \frac{\bar{U}}{U_e}\frac{y\,U_e}{\nu} \tag{4.5}$$

Which leads to this reformulation:

$$\frac{\bar{U}}{U_e} = \frac{1624\,\nu}{y\,U_e} \tag{4.6}$$

By plotting this relation on the same plot of the experimental velocity profile, the two curves are intersected at the point $\tilde{y}^+ = 100$, which corresponds to an ordinate value $\bar{U}(\tilde{y}^+)/U_e$. Noting that $u_\tau = \bar{U}(\tilde{y}^+)/16.24$, the skin friction coefficient can be obtained as follows:

$$c_f = 2\left[\frac{1}{16.24}\left(\frac{\bar{U}(\tilde{y}^+)}{U_e}\right)\right]^2 \tag{4.7}$$

Once the c_f is obtained, the wall shear stress τ_w and the friction velocity u_τ can be computed by using Equation (2.15) and Equation (2.14), respectively.

The results of the experimental mean velocity profiles in wall units are therefore shown in Figure 4.7 for the particular streamwise position of $x = 0$ mm. The first thing to note is the fair agreement with the Spalding's law in the logarithmic region, which confirms the turbulent nature of the velocity profiles. A little deflection from Spalding's law for $y^+ > 300$ can be noted, as the velocity profiles approach to the outer layer. Finally, the velocity values reach a plateau for $y^+ > 10^3$, representing the velocity region outside the boundary layer.

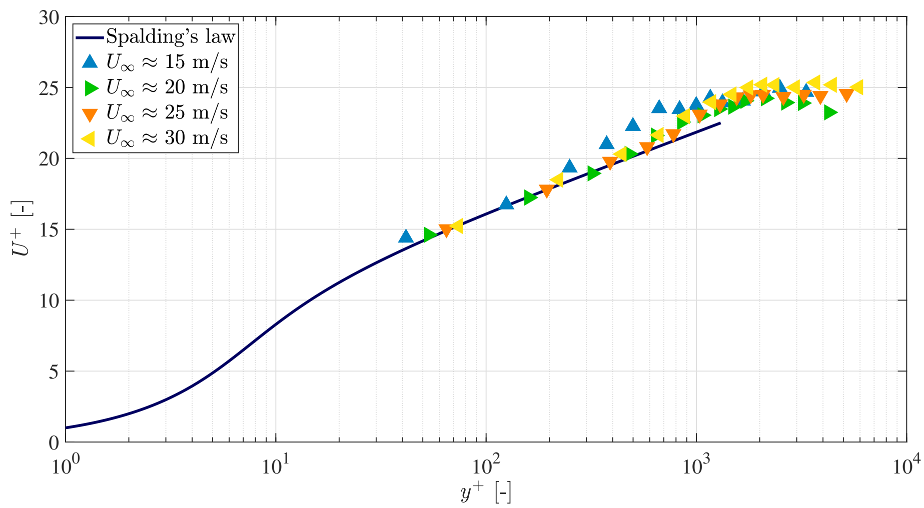

Figure 4.7: Mean velocity profiles in wall units over the antenna in station 2 for the different operating points of interest at $x = 0$ mm, compared with Spalding's law.

An important thing to note is that the experimental campaign achieved velocity measurements until the beginning of the logarithmic region, as the closest points measured at $y = 1$ mm from the wall are situated above $y^+ = 30$. This represents a limitation of the hot-wire system that can be improved in the future, in order to allow velocity measurements in the buffer and inner layer.

Another important analysis concerns the Turbulence Intensity (TI) of the velocity profiles. This quantity can be defined with respect to external velocity U_e:

$$TI = \frac{U'_{rms}}{U_e} \tag{4.8}$$

Where U'_{rms} is the root mean square of the velocity fluctuations U'. The results of the TI profiles are depicted in Figure 4.8 for the particular streamwise position of $x = 0$ mm. The trend of the TI profiles is in line with the physics of the TBL: indeed, the maximum values are reached within the inner layer region, while a drastic reduction towards the external flow is present. A maximum value of 8.5% is reached in the logarithmic layer, while the free-stream turbulence intensity is approximately below 1%.

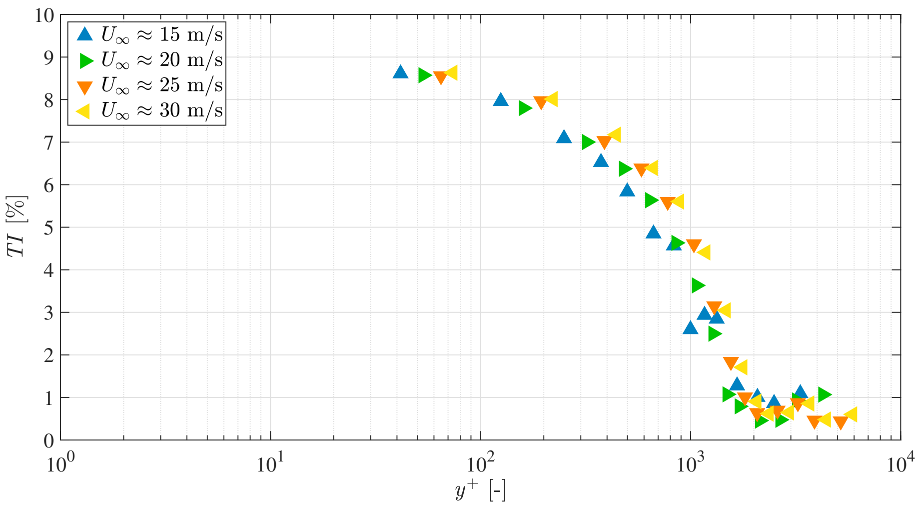

Figure 4.8: Turbulence Intensity profiles expressed in percentage over the antenna in station 2 for the different operating points of interest at $x = 0$ mm.

In conclusion, the hot-wire measurements performed in WAABLIEF facility prove to be successful and interesting results have been obtained. However, an important discrepancy between the inlet velocities U_∞ and the external velocities U_e has been noted during the post-processing. In particular, U_e turns out to be smaller than the U_∞ and this difference increases for higher velocities, as shown in Table 4.2. This is not an expected result, and the problem may again be due to the blockage and total pressure loss caused by the hot-wire system. Further investigations will be needed for future works in order to fully understand the nature of this problem.

As wall-pressure measurements have been performed without the hot-wire system mounted in the test section, the flow field over the antenna is probably different between the hot-wire and wall-pressure campaigns. By looking at Table 4.2, only the case at $U_\infty \approx 15$ m/s can be considered in agreement with the flow field during wall-pressure measurements: indeed, the discrepancy is not as important as the other cases. This is

U_∞ [m/s]	U_e [m/s]
15.39	15.085
19.86	19.09
24.99	23.484
29.97	27.556

Table 4.2: Discrepancy between inlet velocities and external velocities in station 2 for the different points of interest at $x = 0$ mm, observed during hot-wire measurements.

probably due to the fact that blockage effect and total pressure loss are more significant as the flow velocity increases. For this reason, only hot-wire measurements for the case $U_\infty \approx 15$ m/s have been considered for WPS normalization, but different strategies to solve the problem will be needed to improve the present work in the future. The TBL parameters needed for WPS normalization in the case of $U_\infty \approx 15$ m/s are shown in Table 4.3 for the six streamwise positions of interest.

Positions x [mm]	$x = 0$	$x = 2$	$x = 4$	$x = 8$	$x = 14$	$x = 20$
U_e [m/s]	15.085	15.324	15.233	15.229	15.251	15.015
δ [mm]	27.169	25.88	29.758	30.274	30.078	29.067
δ^* [mm]	3.54	3.982	4.7	4.789	5.097	5.371
θ [m]	2.286	2.711	3.331	3.412	3.691	3.856
H [-]	1.548	1.469	1.411	1.403	1.381	1.393
c_f [-]	0.00334	0.00343	0.00332	0.00351	0.0035	0.003
τ_w [Pa]	0.461	0.488	0.466	0.493	0.492	0.41
u_τ [m/s]	0.617	0.635	0.621	0.638	0.638	0.582
R_T [-]	46.194	45.87	50.735	54.624	54.079	44.204

Table 4.3: TBL parameters in the case $U_\infty \approx 15$ m/s for the six streamwise positions of interest.

Chapter 5

Results for wall-pressure measurements

5.1 Dynamic calibration results

In this Section, the results of the dynamic calibration of the electret microphone in the L-shaped array are presented. In particular, a parametric study for the calibration input signal is described to find the best transfer function possible. Moreover, the elaboration of the final transfer function is exposed along with some refinements for its improvement, and the stability of the TF is analyzed.

5.1.1 Parametric study for the calibration input signal

The dynamic calibration of the electret microphones requires an input signal to generate an acoustic field through the loudspeaker into the calibrator device, as already explained in Subsection 3.4.1. With the Agilent Generator, a wide variety of signals can be generated and regulated in amplitude. It is therefore opportune to investigate the effect of the various signal parameters on the final transfer function, in order to choose the signal that leads to the best TF possible.

In the present work, two different types of calibration signals have been considered:

1. The chirp is a signal that produces a frequency sweep with time, spanning from a starting frequency up to a final frequency. Four parameters can be modified in this type of signal: sweep duration, starting and final frequency, and sweep type. The latter can be linear, in which the same amount of time is spent on each frequency, or logarithmic, where the sweep velocity increases with a logarithmic rate.

2. The white noise is a random signal that have equal intensity at different frequencies. The distribution of the frequency with time is completely random and uncorrelated.

Five different signals have been chosen for the parametric study: linear chirp with a sweep duration of 1 and 3 seconds, logarithmic chirp with a sweep duration of 1 and 3 seconds, and the white noise. The frequency sweep for the chirp signals span from 100 Hz to 15 kHz, which represents a wide range where only plane wave propagation is allowed in the calibrator device. The amplitudes of the signals have been set on the Agilent as 500 mVPP (Peak-to-Peak Voltage) for chirp signals and 2 VPP for white noise. Five different dynamic calibrations have been therefore performed, one for each input signal. In order to avoid any other variation that could affect the transfer function, all the input signals of each step of the calibration have been used with the same calibrator position on the microphone to calibrate.

The electret number 6 has been chosen as the representive microphone for the analysis because of its central position on the antenna and on the L-shaped array, which make it the most important microphone on the array. Indeed, it is the first microphone in streamwise direction, therefore it is not in the wake of other microphones. Furthermore, its position is strategic to see the spatial cross-coherence trend along streamwise and spanwise direction.

For the acquisitions, a sampling frequency of $f_s = 51.2$ kHz and an acquisition time of $t_s = 30$ s have been set. The very high value of f_s ensures that Nyquist's rule $f_s \geq 2\, f_{max}$ is respected, and therefore signal aliasing is avoided. Moreover, the gain for the B&K microphones has been set to 316 mV/Pa, while the electret gain selected is 1. In the post-processing, the transfer functions (double-sided) of the two steps were obtained by using the MATLAB function "tfestimate", which computes the TF with Welch's periodogram spectral averaging procedure. Welch's method has been applied with a hanning window of 2^{11} samples, 2^{12} DFT points and 50% overlap. The final transfer function is then obtained by using Equation (3.12).

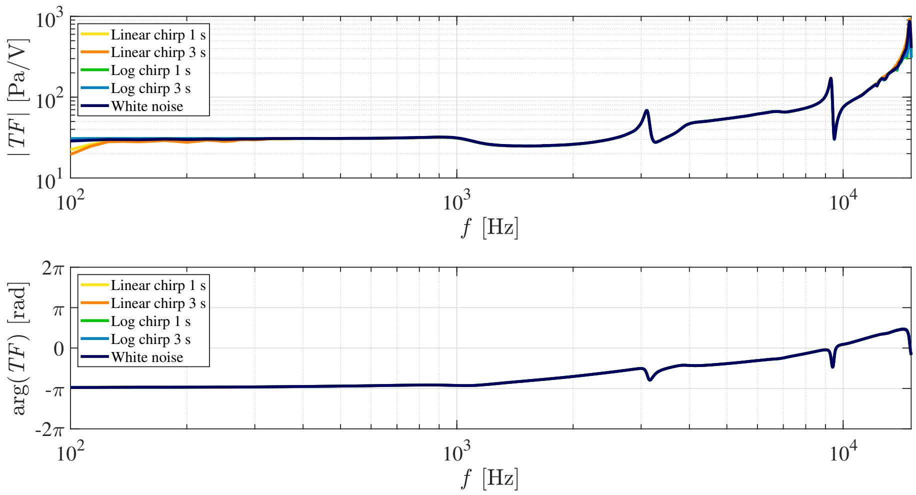

Figure 5.1: Amplitude (top) and phase angle (bottom) of the transfer function between reference B&K microphone and electret number 6 for different calibration input signals.

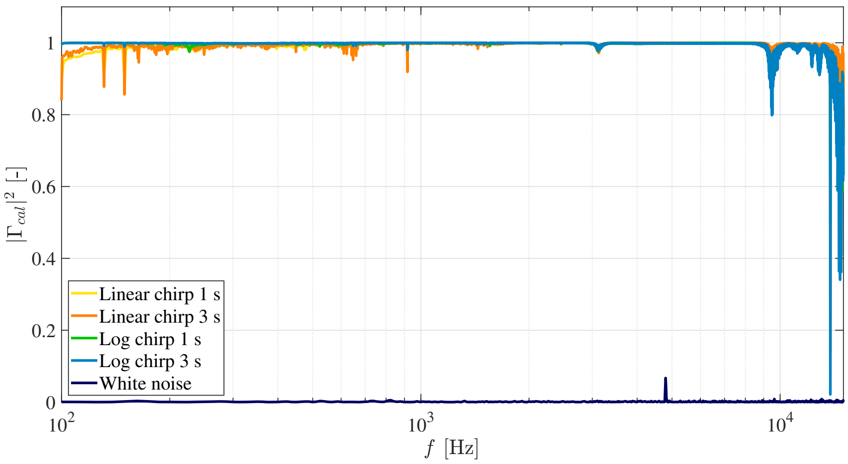

Figure 5.2: Magnitude-squared cross-coherence between the calibrator signals during step 1 and step 2 acquisitions for the different calibration input signals considered.

The results of the transfer functions in frequency domain from the five different calibrations are shown in Figure 5.1. The trends of amplitude and phase angle of the five transfer functions turn out to be similar to each other and in agreement with the results obtained by Van de Wyer et al. [2]. However, some differences between the five calibrations are present, and therefore some considerations can be made:

- For both the linear chirp signals, a drop around 100 Hz can be observed by focusing on the amplitude of the TF. This behaviour is spurious and not in line with the flat response of the transfer function. For this reason, although the linear chirp signals have the smoothest trend at frequencies above 13 kHz, they have been discarded from the final choice. Indeed, in aerodynamics low frequencies are more relevant than frequencies above 13 kHz, therefore a flat response in the low-frequency range was preferred.

- The white noise signal led to good results in terms of flat response, but represents the more approximate solution out of the five cases considered. Indeed, Equation (3.12) is obtained with the assumption of having the same acoustic field during step 1 and 2 of calibration. However, as the acoustic field generated by white noise is random and uncorrelated by definition, it will never be the same during the two steps of calibration. This concept is demonstrated in Figure 5.2, where the magnitude-squared cross-coherence between the calibrator signals during step 1 and 2 is showed for each input signal considered. As the chirp signals are constant and repeatable, the acoustic field sensed by the calibrator microphone in the two steps is basically the same and therefore the cross-coherence is equal to 1 in almost the entire frequency range of interest, while it is equal to zero for the white noise signal. For this purpose, the assumption made in Equation (3.12) is not well respected for the white noise signal, and hence it has been discarded from the final choice.

The final input signal has therefore been chosen between the two logarithmic chirp signals. The two solutions are both a valid choice, since they present very similar trends along the entire frequency range. However, during dynamic calibration it is better to repeat the whole sweep multiple times, in order to have several acquisitions for each frequency. Within a 30-second acquisition time, the 1-second signal is repeated 30 times while the 3-second signal only 10 times. In order to have the same repetitions, the 3-second signal must be acquired for 90 seconds, which means an higher probability to have external noise that could contaminate the acoustic signal. For this reason, the 1-second logarithmic chirp signal has finally been chosen as the calibration input signal.

5.1.2 Elaboration of the final transfer function

The dynamic calibration of the 16 electret microphones of the L-shaped array can be therefore performed by using the 1-second logarithmic chirp chosen from the parametric study. The gains for the microphones and the acquisition and post-processing parameters for the calibration are already described in Subsection 5.1.1. The results of amplitude and phase angle of the transfer functions for the 16 electret microphones are shown in Figure 5.3.

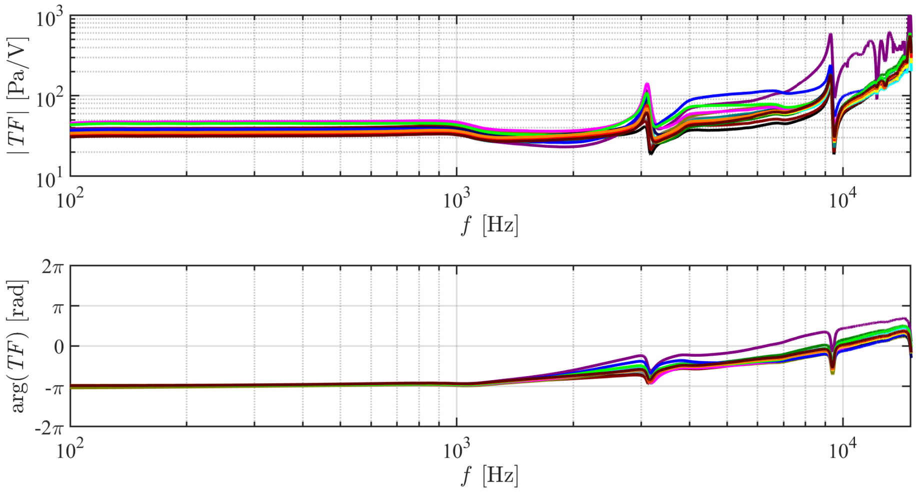

Figure 5.3: Amplitude (top) and phase angle (bottom) of the transfer functions between reference B&K microphone and the 16 electrets of the L-shaped microphone array.

The first thing to note is that the transfer functions are not equal to each other, although they possess the same generic trend. This result remarks the necessity to perform singular calibration for each electret microphone of the L-shaped array.

Moreover, all the transfer functions exhibit evident wiggles around 3 kHz and 9 kHz, especially for the amplitude. This common behaviour is clearly unwanted and depends on the geometrical configuration of the calibrator device. Indeed, it is possible that a destructive interference for those frequencies occurs at the exact radial position of the calibrator lateral channel, leading to pressure change in the calibrator port while the pressure sensed by the microphone to calibrate is not changing [2]. In order to avoid the unwanted oscillations, an alternative computation of the final transfer function has been analyzed, using the Agilent signal that is sent to the loudspeaker as the intermediate signal of the calibration. The comparison of the transfer functions computed with the calibrator and Agilent signal as intermediate is illustrated in Figure 5.4 for the case of electret number 6 of the microphone array.

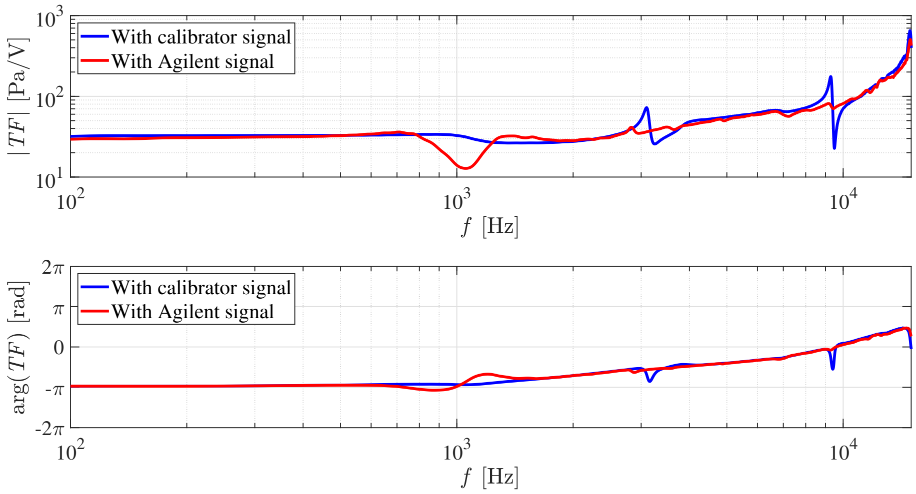

Figure 5.4: Comparison between the transfer functions computed with calibrator and Agilent signal as intermediate for electret number 6.

By looking at the transfer function computed with the Agilent signal, it can be seen that the wiggles at 3 kHz and 9 kHz are avoided. This result is due to the Agilent signal insensitivity to acoustic changes in the calibration port. However, this method introduces a new drop around 900 Hz that is not present by using the calibrator microphone as intermediate signal.

Since it is clear that the use of the calibrator or Agilent signal promotes the low- and high-frequency range respectively, it is reasonable to use a mixed calibration strategy. The idea is to use the calibrator microphone as intermediate signal for frequencies up to a frequency arbitrarily fixed at 2.5 kHz, and the Agilent signal above that frequency. The fixed frequency is chosen properly to avoid the unwanted oscillations of both cases while having a good continuity of the function while passing from one method to the other. The mixed calibration strategy proves to be a winning solution for all the 16 electret microphones of the L-shaped array, as shown in Figure 5.5.

Although the unwanted oscillations at 3 and 9 kHz are removed by using the Agilent signal as intermediate for frequency above 2.5 kHz, the transfer functions obtained in this frequency range is moderately contaminated by spurious peaks associated with electronic parasites. A smoothed version of the transfer functions has therefore been computed to remove the spurious waves caused by the Agilent signal. The result

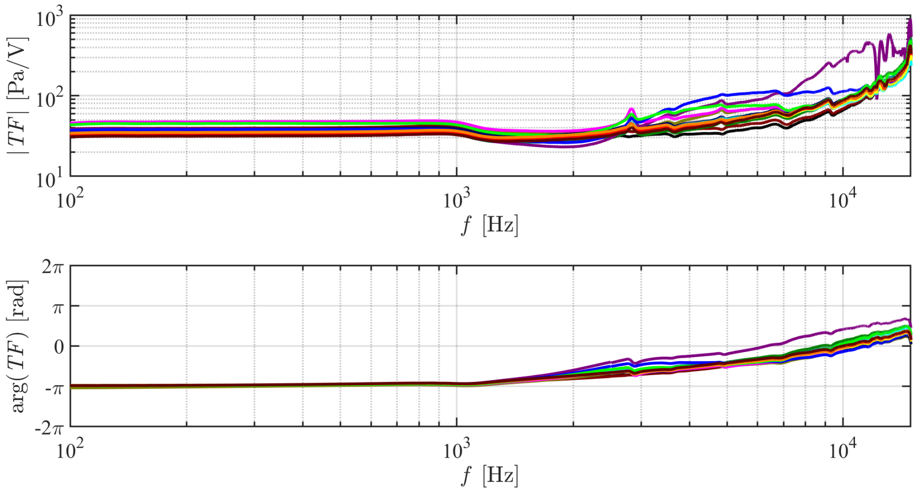

Figure 5.5: Amplitude (top) and phase angle (bottom) of the transfer functions for the 16 electrets of the L-shaped microphone array, computed by following the mixed calibration strategy.

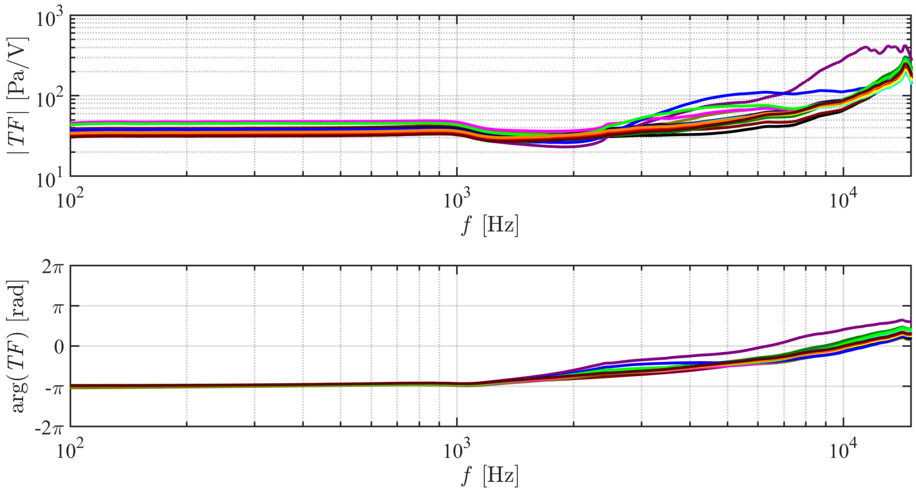

Figure 5.6: Amplitude (top) and phase angle (bottom) of the smoothed final transfer functions for the 16 electrets of the L-shaped microphone array.

of the smoothening procedure is shown Figure 5.6, which illustrates the final transfer functions of the 16 electret microphones of the L-shaped array used for the wind tunnel measurements.

In conclusion, the transfer functions obtained with the mixed calibration and the smoothening procedure turn out to be perfect for the wall-pressure spectra analysis, as they are devoid of unwanted wiggles and spurious peaks. The winning calibration strategy for the electret microphones allow to account for the calibrator acoustic behaviour while expanding the usable frequency range up to 15 kHz.

5.1.3 Stability of the transfer function

As the electret microphones are the cheapest on the market, their frequency response may change over the days due to external conditions, such as ambient temperature and pressure changes, air humidity, etc. For this reason, it is appropriate to analyze the transfer function stability. For this study, the transfer functions from two different calibration days are compared, in order to see the variability of the TF in two different days. In particular, the two days analyzed are the one of the wall-pressure measurements in wind tunnel and the day before.

The results of the analysis are shown in Figure 5.7. For clarity of the figure, only the amplitude of the three most variable transfer functions are depicted, that are the ones of electrets number 2, 3 and 5. Although the TF of each electret preserves its form over the days, significant variations can be easily noted from the graph, especially in the high-frequency range. The highest percentage change with reference to the measurement day is about 25% at around 14.4 kHz for the electret 3. Consequently, the dynamic calibration of the electret microphones must be performed every day in which a wall-pressure measurements campaign is scheduled.

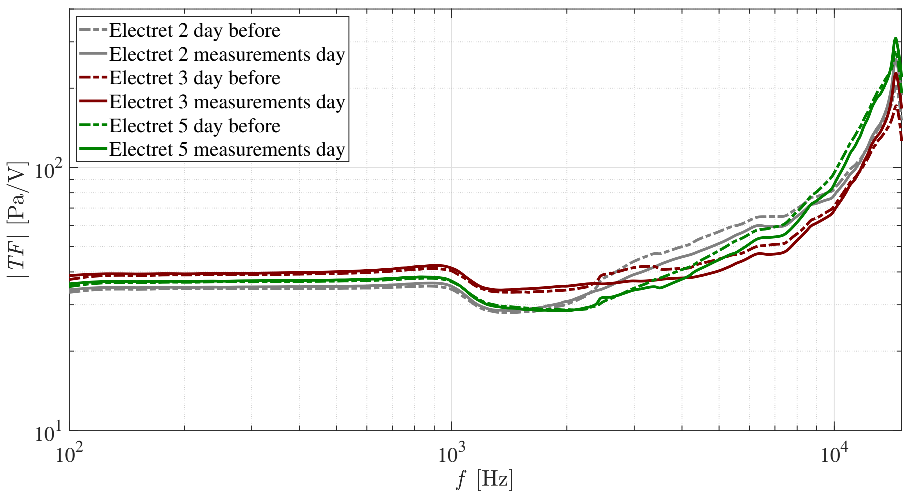

Figure 5.7: Stability of the transfer function over two different days for electrets number 2, 3 and 5.

5.2 Wind tunnel results

Once the dynamic calibration of the electret microphones in the L-shaped array is completed, the wall-pressure measurements in station 2 of the test section can be performed for the four operating points considered in the present work by following the measurement chain already explained in Subsection 3.4.2.

For the acquisitions, a sampling frequency of $f_s = 51.2$ kHz and an acquisition time of $t_s = 60$ s have been set. The gain set in the amplifier for the 16 electret microphones of the L-shaped array is 1, which is the same of the calibration procedure in order to avoid discrepancies in the orders of magnitude when using the transfer functions.

In the post-processing, the application of the calibration transfer functions involves the multiplication of the raw signal acquired in wind tunnel by the electret microphone and its relative TF. However, some operations must be done for this procedure:

- The transfer functions are in frequency domain, while the raw data in Volts acquired in wind tunnel are in time domain. For this reason, the Fourier transform of the electret signal must be computed in order to multiply the two quantities in the same domain. The Fourier transform (double-sided) has been determined by using the MATLAB function "fft", which computes the DFT with a Fast Fourier Transform (FFT) algorithm.
- As the TF and FFT are both computed double-sided, they are expressed in the same frequency domain, which is fundamental for the multiplication. Hovewer, the number of discrete points of the two quantities are different, therefore a transfer function interpolation is necessary to match the same points of the FFT.
- After the multiplication, the calibrated signal in frequency domain of the electret microphone is obtained. As the raw signal has Volt unit and the transfer function has [Pa/V] unit, the calibrated signal is therefore in Pascals. However, the calibrated time-series is needed for the wall-pressure spectra analysis, hence the inverse fourier Transform is applied to the signal. The latter is computed by using the MATLAB function "ifft", which represents the inverse operation of "fft" function.

Once the calibrated time-series in Pascals is obtained, the quantities of interest for the wall-pressure spectra analysis are computed as follows:

- The power spectral density $\Phi_{pp}(f)$ (single-sided) is obtained by using the MATLAB function "pwelch", which returns the PSD in the sense of Welch's periodogram spectral averaging procedure. Welch's method has been applied with a hanning window of 2^{15} samples, 2^{16} DFT points and 50% overlap.
- The cross-coherence function $\Gamma_{pp}(x, z, f)$ (single-sided) is evaluated in the sense of magnitude-squared cross-coherence by using the MATLAB function "mscohere", which in turn uses Welch's overlapped averaged periodogram method. Welch's method has been applied with a hanning window of 2^{11} samples, 2^{12} DFT points and 50% overlap.

In this Section, a brief overview of an electrical problem observed during the experimental campaign is explained along with the strategy to avoid it. Moreover, the saturation of acquisition chain and microphones is introduced, in order to verify the reliability of the data acquired. Finally, the results of the wall-pressure spectra analysis with the comparison with the statistical models are exposed.

5.2.1 Electrical contamination problem

During the experimental campaign, a problem of background noise pollution occured. Indeed, by acquiring the background noise signal and the time-series for the operating points of interest, a contamination of the signal has been found in some acquisitions. An example of this problem is shown in Figure 5.8 for electret number 11 in the case of $U_\infty \approx 15$ m/s, where it is evident that the background noise contaminates the trend of the wall-pressure auto-power spectrum, especially at frequencies below 200 Hz and above 10 kHz.

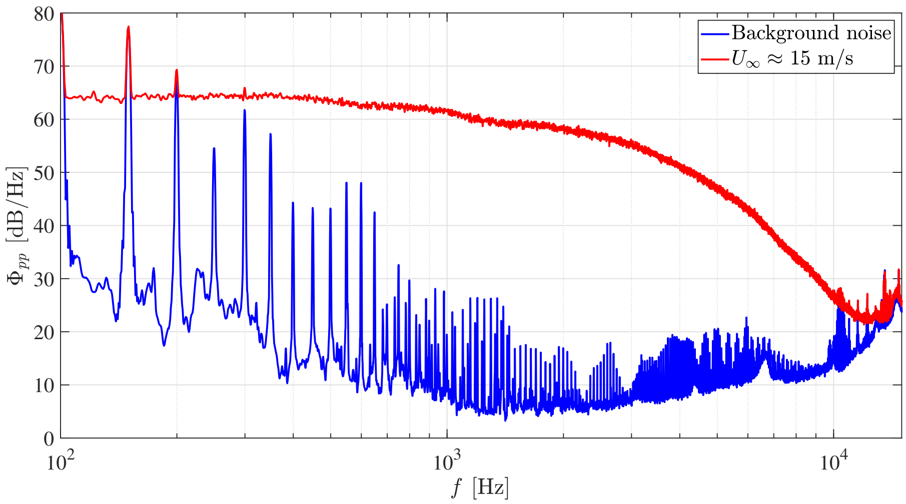

Figure 5.8: Contamination of the auto-power spectrum by background noise for electret number 11 in the case of $U_\infty \approx 15$ m/s.

By looking at the background noise spectrum in Figure 5.8, it can be noted that the highest peaks are periodically repetead every 50 Hz in the spectrum. This is a sign that pollution may come from the electrical network, as the utility frequency of the alternating current that supplies the measurement chain is exactly 50 Hz. In particular, the electrical noise affects some channels of the electret amplifier, making them unusable for the experimental campaign.

After a closer examination, seven channels of the electret amplifier turned out to be unusable because of electrical noise contamination, while nine channels can be considered available for the measurements. After several attempts of reducing the electrical pollution, no solution has been found. As a consequence, the seven polluted channels must be discarded from the measurement chain and therefore only nine electret microphones can be used simultaneously for the experimental campaign in wind tunnel.

In order still to obtain interesting results after the inconvience, a strategical selection of the microphones to plug into the nine unpolluted channels of the amplifier must be made. The selection has been made by thinking about the spatial coherence decay: indeed, in order to see the cross-coherence trend in streamwise and spanwise direction, the most reasonable choice is to choose the central microphone number 6 as reference and eight other microphones in streamwise and spanwise direction. As an exponential decay is expected, it is important to have more microphones near the reference and less towards the ends of the L-shaped array. The nine microphones selected for the WPS analysis are therefore electrets number 1, 4, 5, 6, 7, 8, 10, 13 and 16, as shown in Figure 5.9.

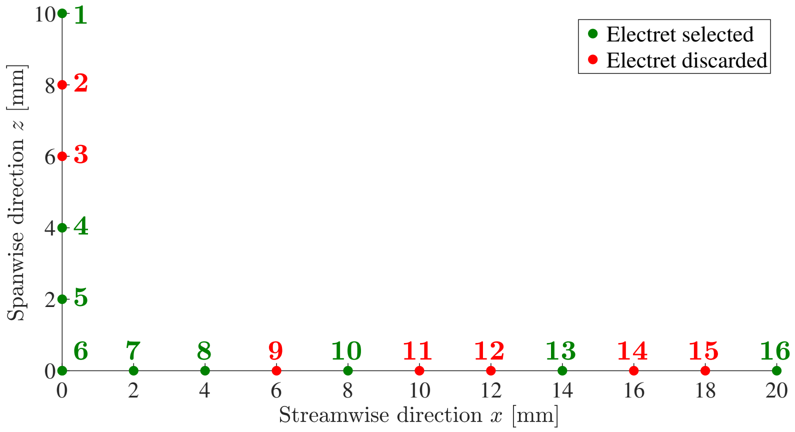

Figure 5.9: Schematic view of the electrets of the L-shaped microphone array selected and discarded for the WPS analysis in wind tunnel.

This strategy has allowed still to obtain reliable and interesting results for the WPS analysis. However, although most of the electrical noise is avoided by using the nine channels available, the pollution of wall-pressure spectra is still present for frequencies above 10 kHz. For this reason, the results for frequencies above 10 kHz has been discarded from the final WPS analysis. The frequency range of interest of the present work therefore spans from 100 Hz to 10 kHz.

5.2.2 Saturation examination

If a sensor is saturated, the data acquired are meaningless and inconsistent with physical reality. For this reason, before starting the post-processing of the data acquired from the electret microphones in the test section, a saturation examination is necessary to check the reliability of the measurements. Two types of saturation exist on experimental field, which are saturation of the acquisition chain and physical saturation of the sensor. The two types of saturation are explained and verified below.

Saturation of the acquisition chain

Saturation of the acquisition chain occurs when the signal to acquire exceeds the maximum voltage that the acquisition chain can handle. In the present work, the voltage range of the acquisition chain spans between -5 and 5 V, therefore the raw signal acquired must not exceed it in order to avoid saturation of the acquisition chain. Since the amplitude of electret signal can be regulated by changing the gain, saturation of the acquisition chain can be easily avoided by setting the proper gain on the electret amplifier.

As wall-pressure fluctuations are more intense while flow velocity increases, the signal amplitude of the microphones is wider for higher velocities. It is therefore opportune to check the saturation for the most critical operating point of interest, that is $U_\infty \approx 30$ m/s. Two different electret gains have been tested in this case: 1 and 10. Although a higher amplitude leads to a better digital resolution of the signal, a gain equal to 10 produces a signal that exceeds ± 5 V. For this reason, the only suitable gain for the most critical case of $U_\infty \approx 30$ m/s is equal to 1.

The raw time-series of electret number 6 acquired with gain 1 is shown in Figure 5.10. The signal amplitude is much narrower than the maximum range of ± 5 V, and this is valid for all the microphones of the L-shaped array. Despite having less digital resolution, saturation of acquisition chain has thus been widely avoided.

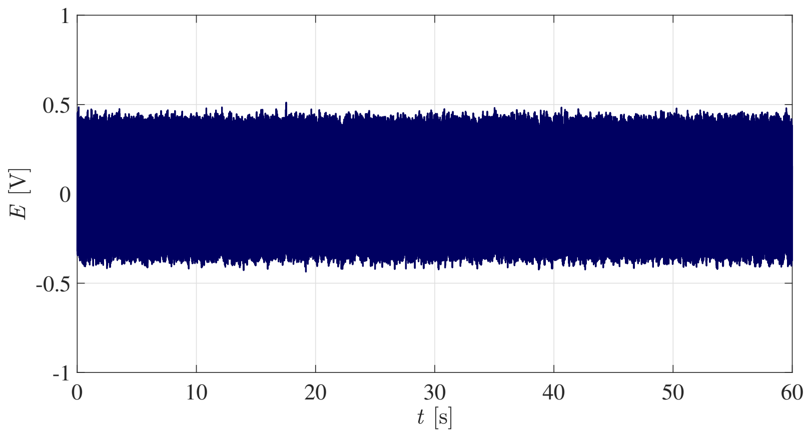

Figure 5.10: Raw time-series of electret number 6 for $U_\infty \approx 30$ m/s, acquired with gain 1 of the electret amplifier.

Physical saturation

Physical saturation occurs when the pressure level to measure exceeds the maximum level measurable by the sensor. This type of saturation is a much more complex phenomenon than saturation of the acquisition chain, therefore it is more difficult to detect and deal with. When a microphone is physically saturated, there is no solution to solve the problem rather than changing flow conditions, which means modifying the experimental campaign.

There is no specific rule to verify the physical saturation of an electret microphone. As a rule of thumb from the experimental experience of the members of the VKI Aeroacoustics Team, the maximum SPL measurable by an electret microphone is equal to 110 dB. By using Equation (2.24), the SPLs of the calibrated time-series acquired from the nine electret microphones of the L-shaped array have been computed. The maximum SPL for the most critical operating point of interest ($U_\infty \approx 30$ m/s) has been reached by electret number 16, with a value of 108.565 dB. As the latter is still below the maximum value of 110 dB, physical saturation of the sensor has been avoided as well.

5.2.3 Wall-pressure spectra analysis

After verifying the reliability of the data acquired by checking the saturation, the wall-pressure spectra analysis can be finally carried out. The calibrated signals of the nine electret microphones selected in the L-shaped array must be used for the post-processing of WPS quantities.

The first parameter to analyze is the one-point power spectral density of wall-pressure fluctuations $\Phi_{pp}(f)$. No significant variation of the auto-power spectrum trend has been found between the nine electrets of the microphone array. Consequently, electret number 6 has been chosen as the representative microphone for the analysis, as it is the most important microphone of the L-shaped array. The results of PSD for electret number 6 are illustrated in Figure 5.11 for the different inlet velocities and the background noise.

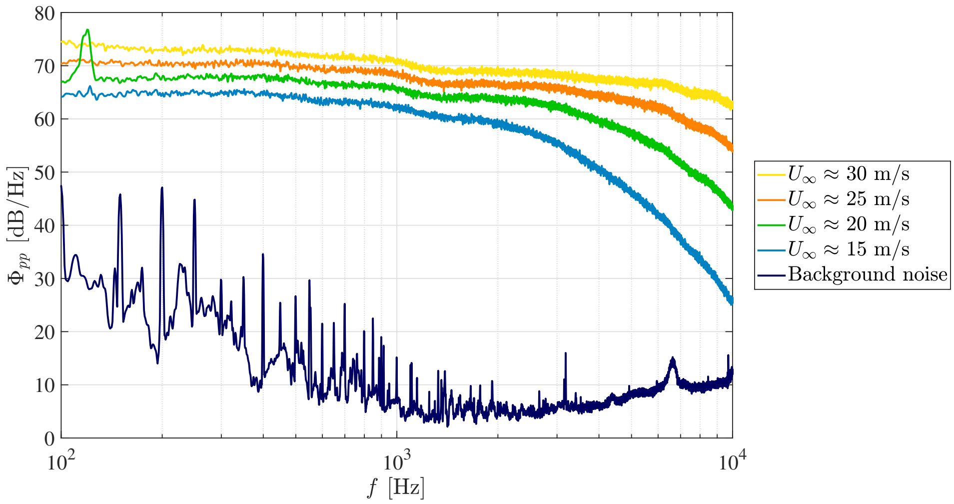

Figure 5.11: Power Spectral Density of electret number 6 for different inlet velocities versus the background noise.

All the spectra display canonical trend, in agreement with WPS of the several works available in literature. The most relevant thing to note is that the PSD enhances as the flow velocity increases, which means that wall-pressure fluctuations in the TBL are more intense at higher velocities. Moreover, by looking at the auto-power spectrum for $U_\infty \approx 20$ m/s, a peak occurs at a frequency around 120 Hz. This behaviour is clearly spurious and is probably due to a resonance frequency of the axial fan of the facility, which excites the PSD for a specific frequency when the operating point of the facility is around 10.5 Hz.

The next task is to normalize the WPS with the TBL parameters in Table 4.3 obtained for the case $U_\infty \approx 15$ m/s, in order to compare the experimental results with the statistical models available in literature.

Regarding the inner-layer scaling, the agreement with the literature is shown in the high-frequency region, as already explained in Section 2.3. The inner-scale normalization of the PSD in the case $U_\infty \approx 15$ m/s for electret number 6 is shown in Figure 5.12 and compared with the ω^{-5} power law in the high-frequency region. The agreement with the theoretical law in the high-frequency region is very good, confirming the fair prediction of the literature for the WPS at high frequencies.

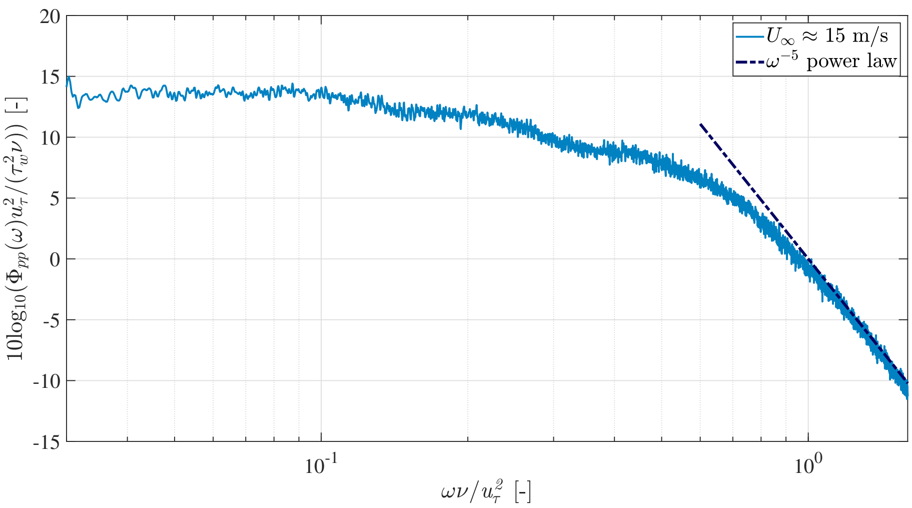

Figure 5.12: Power spectral density of electret number 6 normalized with inner-layer parameters and compared with the ω^{-5} power law in the high-frequency region.

For low- and mid-frequency ranges, the prediction with outer-layer parameters is more complicated to obtain, according to Goody [17]. In the present work, the experimental WPS curve is compared with Chase-Howe's model in Equation (2.33) and Goody's model in Equation (2.35). The results of the outer-scale normalization in the case $U_\infty \approx 15$ m/s for electret number 6 is shown in Figure 5.13, along with the comparison with the two models considered. As the Chase-Howe's model is only a function of $\omega^* = \omega\delta^*/U_e$, the prediction of this model is not reliable. Conversely, the Goody's model agreement is fairly good in the low- and mid-frequency ranges, and the

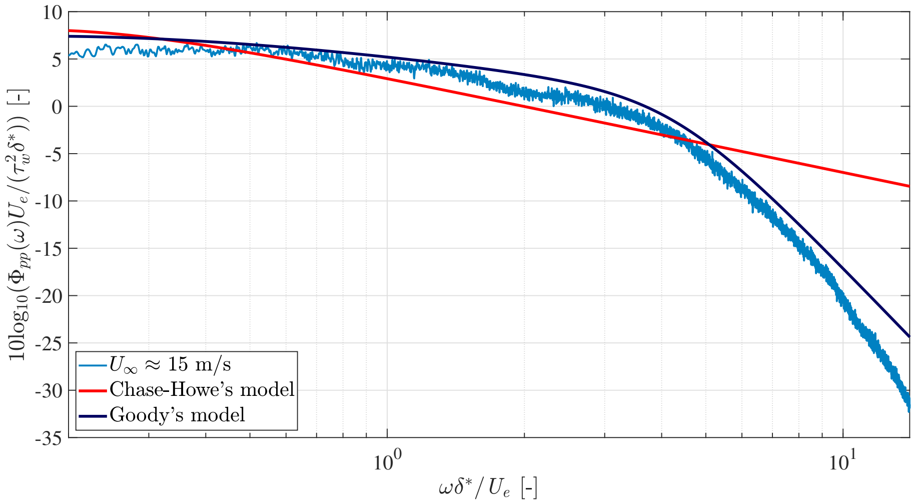

Figure 5.13: Power spectral density of electret number 6 normalized with outer-layer parameters and compared with Chase-Howe's model and Goody's model.

results are very promising for a WPS prediction with ZPG. The contemplation of the Reynolds number effect through the ratio R_T proves to be a winning solution, and the expansion of the WPS database in literature can lead to a fine-tuning of this model.

Regarding the cross-coherence function $\Gamma_{pp}(x, z, f)$, two types of analysis can be studied: the dependency on spatial coordinates x and z and the trend in frequency domain. One of the parameters must be fixed in order to see the cross-coherence as a function of the other parameter. For istance, it is interesting to see the magnitude-squared cross-coherence in frequency domain between central electret number 6 and the adjacent in streamwise direction, that is electret number 7, as shown in Figure 5.14 for the different operating points of interest.

The first thing to note is that the four cases considered possess the same general trend, which is a decay along the frequency range. This means that the characteristic length is lower for high-frequency turbulent structures. Moreover, by focusing on the influence of flow velocity, it can be seen that for lower velocities Γ_{pp} has higher values up to 500 Hz, but decay faster than higher velocities above that frequency.

In order to see the spatial cross-coherence trend, electret number 6 has been chosen as reference position and an arbitrary frequency of $f = 1000$ Hz has been fixed. The results of the spatial magnitude-squared cross-coherence trends in streamwise and spanwise directions are shown in Figure 5.15. A faster decay of spanwise cross-coherence than streamwise can be easily noted, and the same result is exhibited for the entire frequency range. This means that turbulent structures in streamwise direction have higher characteristic length than the ones in spanwise direction. Moreover, a faster streamwise and spanwise decay is observed for lower velocities in the particular case of $f = 1000$ Hz, remarking that for frequencies above 500 Hz the low-velocity cross-coherence decay is faster.

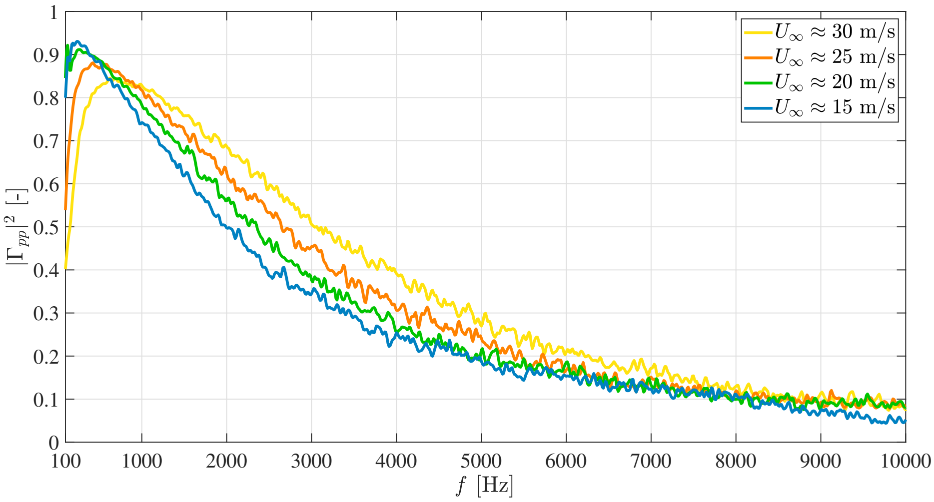

Figure 5.14: Magnitude-squared cross-coherence in frequency domain between electret number 6 and the adjacent microphone in streamwise direction for different inlet velocities.

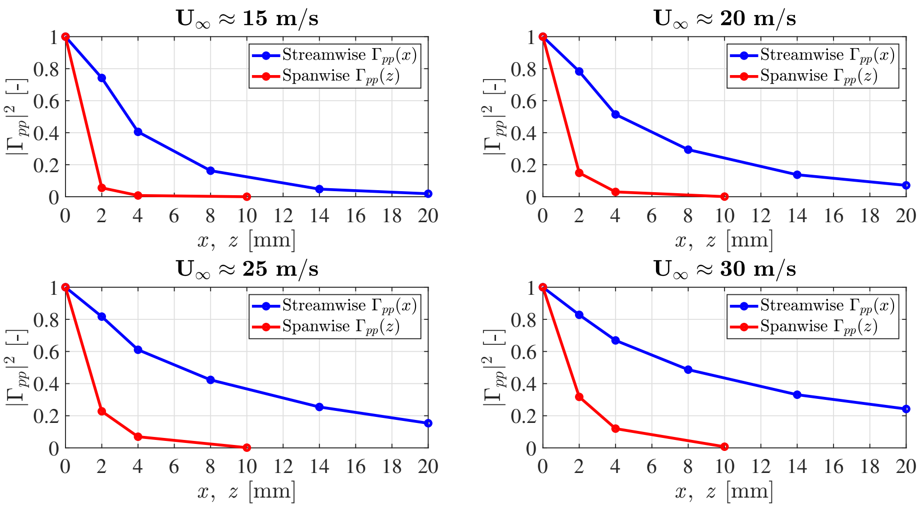

Figure 5.15: Spatial magnitude-squared cross-coherence at $f = 1000$ Hz between electret number 6 and the other microphones in streamwise and spanwise direction for different inlet velocities.

Likewise the auto-power spectrum, it is interesting to compare the experimental results with the models available in literature. In the present work, Corcos' model [21] in Equation (2.36) is used, with α and β revised by Blake [23] for smooth walls and Smol'yakov's model [24] in Equation (2.37) for convection velocity U_c.

The comparison between the experimental cross-coherence in streamwise and spanwise direction with Corcos' model is shown in Figure 5.16 for the case of $U_\infty \approx 15$ m/s at $f = 1000$ Hz. For this particular frequency, the Corcos' model predicted the spatial decay qualitatively well, although an overestimation is present especially for the streamwise decay. This is probably due to an overestimation of the convection velocity with Smol'yakov's model, which is found in the work of Van de Wyer et al. [2] and can affect the prediction of spatial decay.

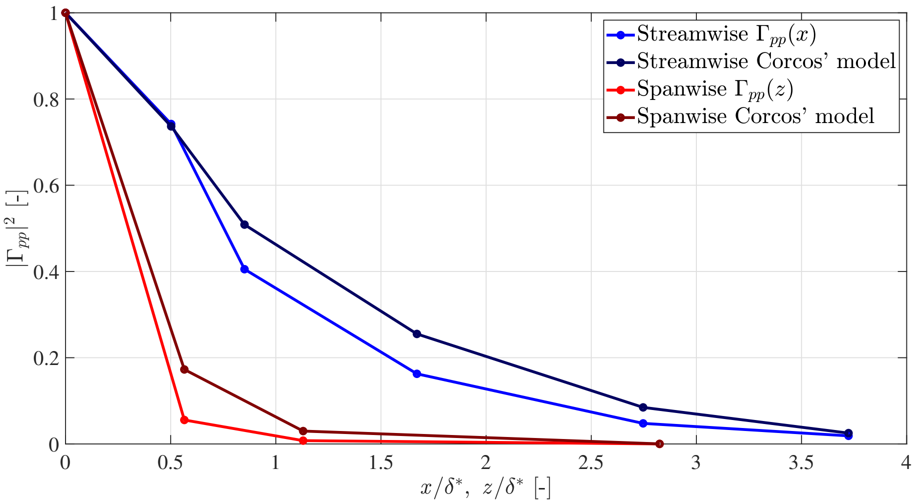

Figure 5.16: Spatial magnitude-squared cross-coherence at $f = 1000$ Hz in streamwise and spanwise direction for the case $U_\infty \approx 15$ m/s, compared with Corcos' model.

In conclusion, despite some problems occured during the measurements, the experimental campaign has led to very promising results especially for the WPS prediction. The results showed general agreement with the statistical models of the literature, which is encouraging for their fine-tuning and improvement. Moreover, the fair accordance of the experimental results is reassuring for the reliability of the data acquired. Future improvements will be possible by examining different flow configurations and other parameters, such as convection velocity or coherence length.

Chapter 6

PIV preliminary measurements

In addition to the official experimental campaign exposed thus far, preliminary Particle Image Velocimetry (PIV) measurements have been conducted. The aim of this work is to explore the feasibility of performing such technique in WAABLIEF facility and evaluate the reliability of the data acquired. PIV technique can improve the characterization of the TBL over the antenna given by hot-wire anemometry, as it provides the information of velocity profiles on the entire velocity field captured by the camera. With the purpose of improving the results obtained in the present work, it is therefore interesting to study the possibility of a future PIV campaign in WAABLIEF facility.

In this Chapter, a brief introduction to PIV technique is exposed, and the optimal experimental set-up that allows PIV measurements for the particular case of WAABLIEF facility is described. Moreover, calibration and post-processing strategies are explained, and finally preliminary results are shown to evaluate the reliability of the data acquired.

6.1 Introduction to PIV

The PIV is an optical-based technique that relies on the measurement of the velocity of tracer particles introduced into the flow. The basic principle is to compute the flow velocity by measuring the displacement of a tracer particle and the time between the initial and final position. The tracer particle must be therefore carried by the flow with the same velocity.

In order to make the tracer particles visible and capture the displacement, a narrow light sheet is generated from a laser, which is synchronized with a camera that records consecutive images of the illuminated particles. The light sheet is moved along the flow field by a prism that reflects the light to illuminate the region of interest, and is regulated in thickness and opening angle by laser sheet optics. The plane of interest is therefore illuminated when the camera is recording, allowing the tracking of the seeding particles on the entire field captured by the camera, which is called Field-Of-View (FOV). A typical PIV experimental set-up for the recording of two velocity components in a plane is shown in Figure 6.1.

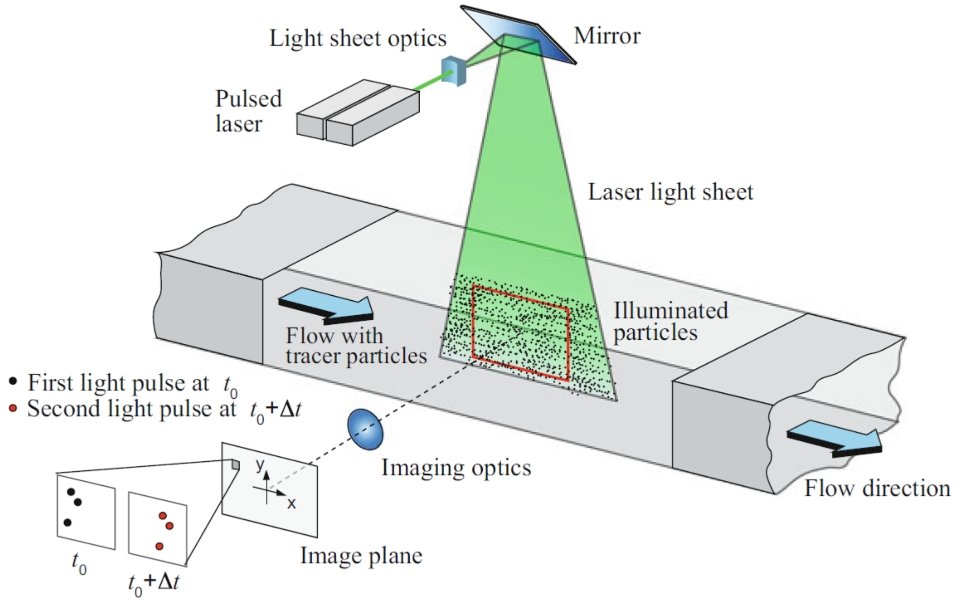

Figure 6.1: Schematic view of the typical experimental arrangement of the PIV system in a wind tunnel [26].

Two main configurations of PIV are available to measure instantaneous velocity fields in the measurement plane, depending on the number of velocity components of interest:

1. The planar 2C-2D PIV is the classical configuration that enables to measure the instantaneous field of the 2D velocity vector on the illuminated plane recorded by the camera. In this configuration, the camera is perpendicular to the light sheet in order to measure the two velocity components that lie on the illuminated plane.

2. The planar 3C-2D PIV, also known as Stereo PIV, is the more complete version of the 2C-2D PIV, as it enables to measure also the third velocity component of the instantaneous velocity field, which is perpendicular to the illuminated plane. This configuration needs two cameras positioned at a certain angle with respect to the light sheet in order to measure the entire 3D velocity vector.

The main advantage of this technique with respect to hot-wire anemometry and Laser Doppler Velocimetry is that the measurement is not punctiform, but includes the entire FOV in the same acquisition. Moreover, it is a non-intrusive method for the flow, in contrast to pressure probes or hot-wires. Furthermore, the high density of velocity vectors in the instantaneous field measured leads to an excellent spatial resolution.

Conversely, the main drawback is related to temporal resolution: indeed, the sampling frequency of image acquisition is limited ($f_s \sim 10$ Hz) due to technological restrictions [26]. This problem is partially solved by using the time-resolved PIV System because it enables higher sampling frequencies ($f_s \sim 2000$ Hz), but the repetition rate is still too low with respect to other velocity measurement techniques, such as hot-wire anemometry. Moreover, an uniform seeding along the flow field is usually difficult to obtain, especially in suction-type wind tunnels, therefore an efficient seeding system must be present.

6.2 PIV experimental set-up and measurement strategies

In the present work, the classical planar 2C-2D PIV has been performed to measure streamwise and upwash components of the velocity vector. For logistical reasons, the preliminary test has been performed in station 1 of the WAABLIEF facility, but these measurements can also be arranged for station 2.

The experimental set-up of a PIV system is typically composed by several subsystems. The experimental arrangement used in the present work is explained in the following:

- The seeding system has the task to introduce tracer particles into the flow. The particle size must be small enough to allow the assumption that the tracers follow the flow, but also large enough to produce scattering for images to be recorded. In practice, tracer particles ranging from 1 to 10 μm are optimal for PIV measurements [15]. The performance of this system is fundamental to have reliable measurements: indeed, the seeding uniformity along the flow is necessary to have a proper tracking of the particles. Concentration and distribution of the seeding particles are therefore the key factors that determine the quality of the measurements.

  During the campaign, some problems of seeding uniformity occured due to the design of the WAABLIEF facility, which is a suction-type wind tunnel. After several attempts, an optimal configuration has been found to obtain a quite uniform seeding in the test section. The system consists of DEHS particles pressurized in a tank, which is connected to a pipe that releases the seeding particles into a mixing box. The latter has the function to create turbulent mixing and homogeneity in the seeding flow, and for this purpose also a homemade turbulence grid has been added at the outlet. The mixing box is therefore placed near the bottom region of the wind tunnel inlet for the injection of seeding particles into the flow. The configuration used for the seeding system is shown in Figure 6.2.

- A pulsed laser has been used to generate a light sheet that illuminates the tracer particles, making them visible for image acquisition. The laser intensity must be regulated to have the optimal value that properly illuminates the tracer particles but does not produce too much light reflection on the bottom wall of the test section. As the 64-microphone antenna is made of steel, the light reflection generated on the surface is too much high to make the measurements feasible.

(a) DEHS pressurized tank (b) Mixing box

Figure 6.2: DEHS pressurized tank (a) and mixing box (b) of the seeding system, placed at the inlet of the WAABLIEF facility. The tank is connected through a tube to a pipe that releases the tracer particles into the mixing box, which directs the seeding flow into the circular bell-mouth inlet of the wind tunnel.

As a preliminary solution, a black paperboard has been placed on station 1 to cover the bottom wall and avoid light reflection.

- Light sheet optics is needed to manage the illuminated plane in thickness and opening angle. During the campaign, a simple optic system composed by a spherical and cilindrical lens has been used. The spherical lens controls the light sheet thickness, while the cylindrical lens manages the opening angle. The position of the lenses with respect to the laser must be regulated to have a thin and wide light sheet.

- The prism has the function to reflect the light sheet into the wind tunnel. The position of the light sheet in the wind tunnel is therefore managed by moving the prism.

- The LaVision Imager Camera has been used for image acquisition. The positioning must be precise in order to have the FOV containing the region of interest and aligned with the bottom wall. The focus of the camera is also important to have high-quality images, as the tracer particles must be well-defined on the image acquired.

- The calibration plate is needed to determine the relation between the displacement of the tracer particles in the image plane and in the real illuminated plane. For this purpose, the calibration plate cointans several 1 mm-diameter black dots distributed all over the surface with 2 mm of spacing in between.

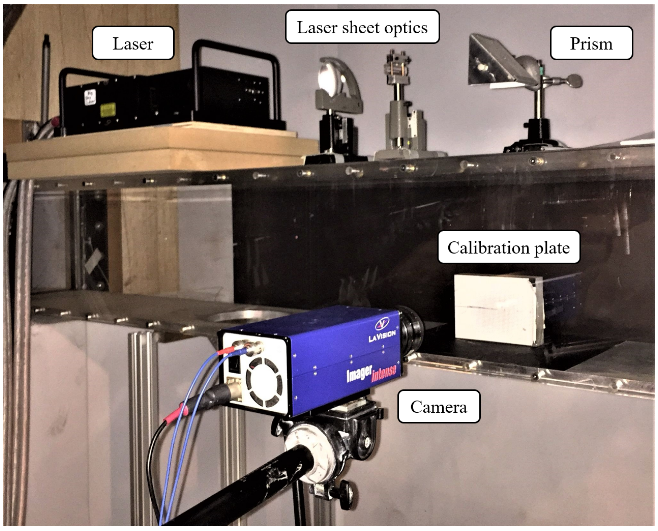

Figure 6.3: Experimental arrangement of the PIV system in station 1 of the WAABLIEF test section.

- Acquisition and post-processing of the images is managed by LaVision Programmable Timing Unit (PTU). This particular computer designed for PIV measurements is connected to the pulsed laser and to the camera and controls the synchronization between the two devices. Indeed, the image acquisition of the camera must occur at the same time of laser pulsation, in order to record the tracer particles at the exact time of illumination. The images are then acquired and post-processed by LaVision DaVis 7 software.

The experimental set-up of the PIV system is therefore quite complex, and each subsystem must be arranged in the proper way to accomplish a good measurement campaign. The final experimental set-up used in the test section for the preliminary campaign is illustrated in Figure 6.3.

6.2.1 Field-of-view calibration

Before the acquisition, it is fundamental to calibrate the field-of-view in order to associate properly the image displacement seen in the image plane to the real displacement in the flow plane. For this purpose, the calibration plate is placed into the wind tunnel for the calibration procedure. The surface of the calibration plate is depicted of black dots of known dimension and position. The aim of the calibration is to find the magnification factor M, which is the ratio between the real length in meters and the length seen on the image plane in pixels. By multiplying it by the displacement in pixels of a tracer particle seen on the image plane, the real displacement on the flow plane is retrieved.

The calibration procedure starts with the positioning of the calibration plate into the region of interest of the test section. The focus of the camera can be adjusted to

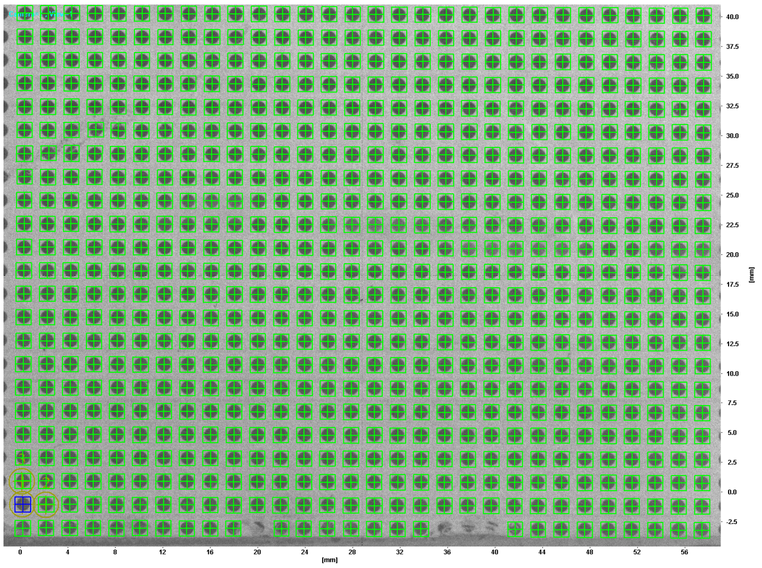

Figure 6.4: Result of the calibration procedure fulfilled by DaVis software on the calibration image. On the left corner, the black dots chosen for the reference system are marked.

enlarge or restrict the FOV, but the camera lens must be well-focused to obtain a clear image of the black dots. Once the calibration set-up is ready, the calibration image can be acquired by using DaVis software. The latter can accomplish the calibration procedure automatically. First, diameter and spacing of the black dots must be inserted as input parameters. Then a dot on the calibration image must be chosen as origin of the reference system along with other two dots to provide axes directions. Finally, the calibration procedure can be launched on DaVis, and the software is able to recognize all the dots present in the FOV and find the magnification factor M. In the present work, a magnification factor of $M = 0.044454$ mm/pixel has been obtained, and the result of the calibration procedure is shown in Figure 6.4.

6.2.2 Image acquisition and post-processing

Once the FOV calibration is completed, PIV measurements of the flow of interest can be performed. The images acquisition is managed by LaVision PTU, which regulates the synchronization between the laser pulse and the camera recording. For the acquisition, it is important to set the right time interval between the first and second laser pulse, which thus corresponds to the time between the two images recorded for particle tracking. The time interval Δt in which the particle displacement in pixels is equal to an arbitrary value d_p is computed using the magnification factor M and the inlet velocity U_∞:

$$\Delta t = \frac{d_p \, M}{U_\infty} \tag{6.1}$$

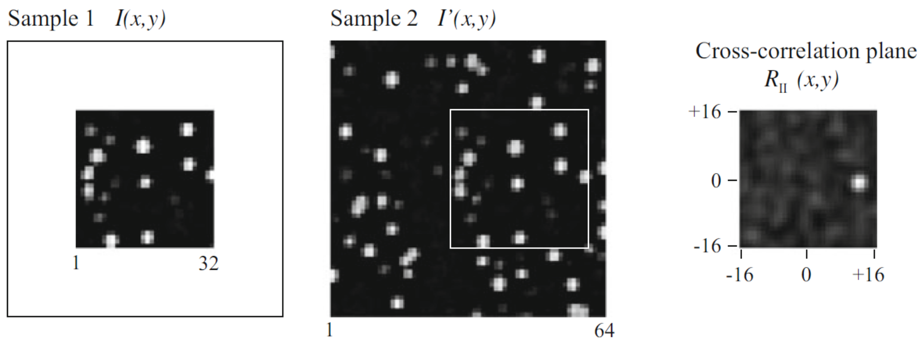

Figure 6.5: Cross-correlation map computed by correlating a sample 1 at the time t with a sample 2 at the time $t + \Delta t$. The peak in the map is visible at approximately 12 pixels to the right [26].

This parameter represents the amount of time between the initial and final position of a tracer particle. As the displacement depends on the flow velocity, the time interval computation must take into account U_∞ to capture a good displacement on the image plane.

Once the time interval and sampling time and frequency are set on the DaVis software, the PIV measurements can finally start with the images acquisition. The raw images acquired are therefore subjected to post-processing in order to retrieve the velocity field. A typical PIV image post-processing is summarized below:

- The image is digitalized using discrete grey levels and divided in interrogation windows, which are defined in dimensions by the operator. Each suddivision must be large enough to contain a sufficient number of tracer particles for the velocity computation, but small enough at the same time to have a detailed description of the flow field and therefore increase the spatial resolution of the measurement. Typical dimensions of the interrogation windows are 64 x 64 or 32 x 32 pixels.

- The displacement of the tracer particles must be computed for each interrogation window. In the case of double frame/single exposure recording technique, the evaluation of the particles displacement is performed through the use of the discrete cross-correlation function for the pixel intensities [26]. For each interrogation window, the template at the time t is "shifted around" in the sample at the time $t + \Delta t$ to produce a cross-correlation map. As the cross-correlation function statistically measures the degree of match between the two samples for a given shift, the highest value of the cross-correlation map is the indication of the most probable displacement. The position of the peak in the map thus represents the displacement vector estimation for the specific interrogation window analyzed. An example of this procedure is shown in Figure 6.5.

- The cross-correlation procedure is performed for all the interrogation windows present in the FOV to obtain the displacement vector field of the tracer particles.

Subsequently, the velocity vector field is computed by using the time interval Δt imposed between the recording of the two images.

In the present work, the entire image post-processing has been managed by DaVis software. By setting window shape and size and other filtering parameters, the software is able to compute the entire FOV velocity field, returning streamwise and wall-normal velocity components u and v for each pair of coordinates (x, y).

6.3 PIV preliminary results

By following the experimental set-up already axplained in Section 6.2, calibration and PIV measurements for the operating points of interest can be performed. Two operating frequencies of the axial fan equal to 8 and 16 Hz, corresponding to $U_\infty \approx 15$ m/s and $U_\infty \approx 30$ m/s respectively, are discussed in the present analysis.

For image acquisition, a sampling frequency of $f_s = 2$ Hz and an acquisition time of $t_s = 150$ s have been set for each operating point, leading to a time-series composed by 300 double-frame images. The seeding pressure has been regulated for each case to have the best seeding uniformity along the test section, and the laser power has been set to 34% of the maximum power. The time interval Δt for each operating point has been computed by considering a fixed pixel displacement of $d_p = 8$ pixels and using Equation (6.1). A time interval equal to 23.54 and 11.74 μs have been found for image acquisition in the case of $U_\infty \approx 15$ m/s and $U_\infty \approx 30$ m/s, respectively.

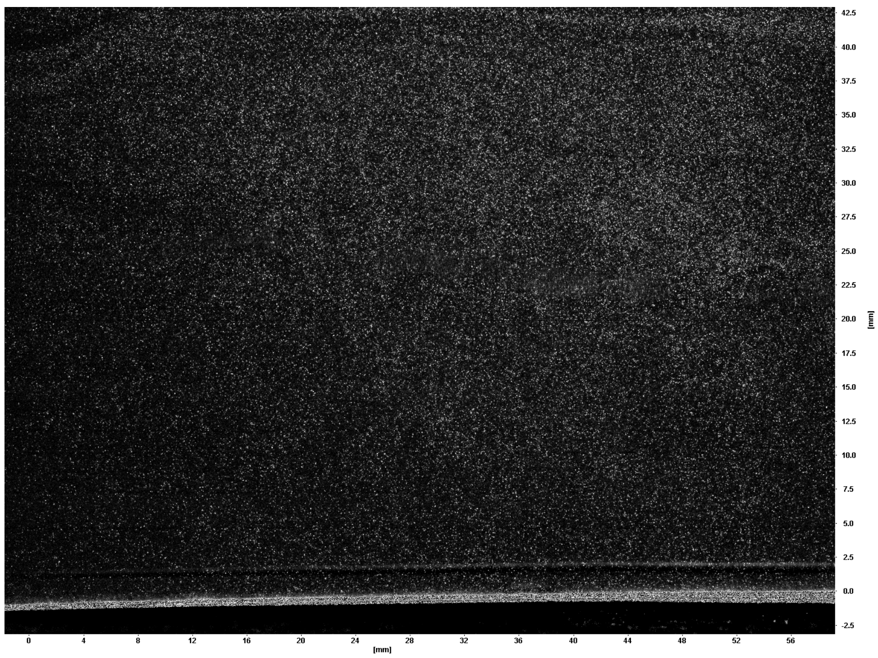

Figure 6.6: Raw image of the FOV containing the tracer particles illuminated by the light sheet.

An example of raw image acquired during the experimental campaign is depicted in Figure 6.6. A quite uniform seeding can be noted in this picture, although the uniformity is dependent on time and flow conditions. In particular, higher flow velocities in the wind tunnel exhibited a more uniform seeding than lower velocities, probably due to a higher turbulent mixing. Moreover, a region with no particles can be noted on the bottom, which represents the wall of the test section. The latter seems to be a bit tilted in the image, which means that the FOV in not straightly aligned with the bottom wall. For this reason, the FOV has been aligned during the post-processing, in order to have the bottom wall straight and coincident with the bottom edge of the FOV.

For the post-processing on DaVis software, a square interrogation window has been set with a decreasing window from 64 x 64 to 16 x 16 pixels and a 50% overlap. The variable window size allows to provide a clearer definition of the velocity field near the bottom wall, which is the most critical region due to very high velocity gradients $\partial u/\partial y$. Finally, the instantaneous velocity field obtained from DaVis software has been post-processed on MATLAB to obtain the statistical parameters of interest.

The results of the mean streamwise component $\bar{u}$ in the entire FOV are shown in Figure 6.7 for the two operating points of interest. The colormaps exhibit a coherent and uniform velocity field that is in line with the typical trend of a velocity profile in a boundary layer. As a consequence, the configuration of seeding system used during the preliminary campaign proves to be successful to characterize the entire FOV.

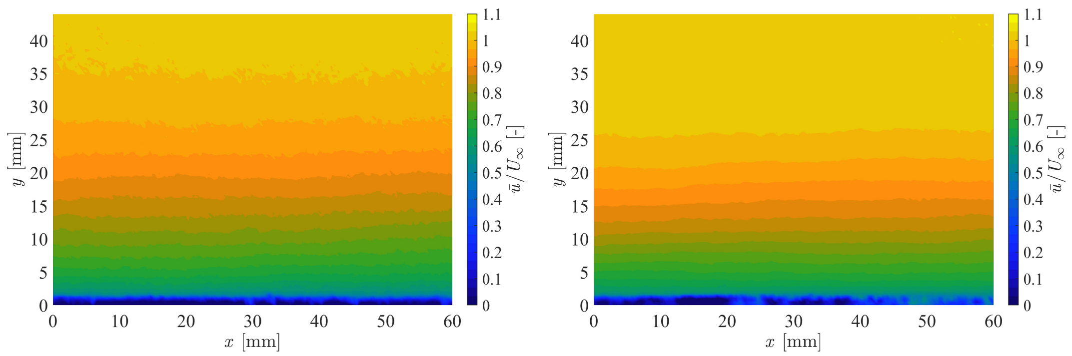

(a) Case $U_\infty \approx 15$ m/s (b) Case $U_\infty \approx 30$ m/s

Figure 6.7: Mean streamwise velocity component in the FOV for $U_\infty \approx 15$ m/s (a) and $U_\infty \approx 30$ m/s (b).

For the mean wall-normal velocity component $\bar{v}$, the results are shown in Figure 6.8. The values for this velocity component turn out to be very small, meaning that the flow is mostly in streamwise direction. As there is no intrusion in the flow, this is the expected result for the wall-normal velocity component.

Moreover, the fluctuating component of the instantaneous velocity field can be analyzed as well. It is interesting to compute the turbulence intensity TI_u of the fluctuating streamwise velocity component, obtained with the inlet velocity U_∞ as

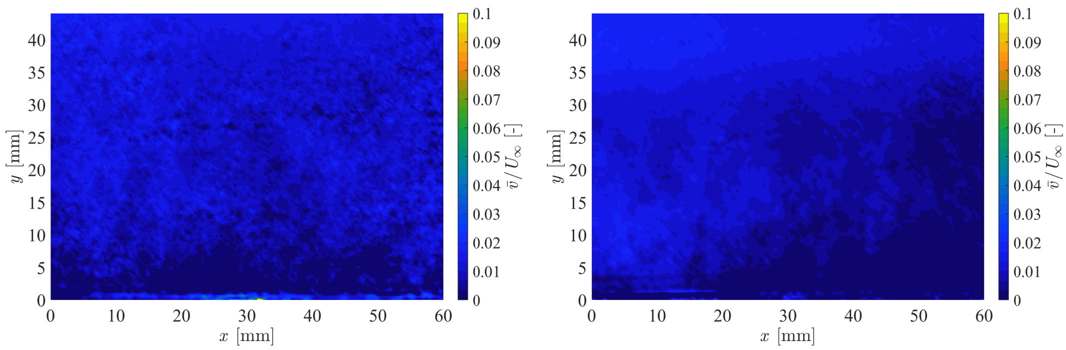

(a) Case $U_\infty \approx 15$ m/s (b) Case $U_\infty \approx 30$ m/s

Figure 6.8: Mean wall-normal velocity component in the FOV for $U_\infty \approx 15$ m/s (a) and $U_\infty \approx 30$ m/s (b).

reference:

$$TI_u = \frac{u'_{rms}}{U_\infty} \tag{6.2}$$

The results of the TI expressed in percentage for the streamwise velocity component are shown in Figure 6.9. The trend of the turbulence intensity in the FOV is coherent and in line with the physics of the TBL: indeed, the highest values are present within the region near to the wall, that is the inner layer, while a drastic reduction of TI can be observed towards the outer region of the boundary layer.

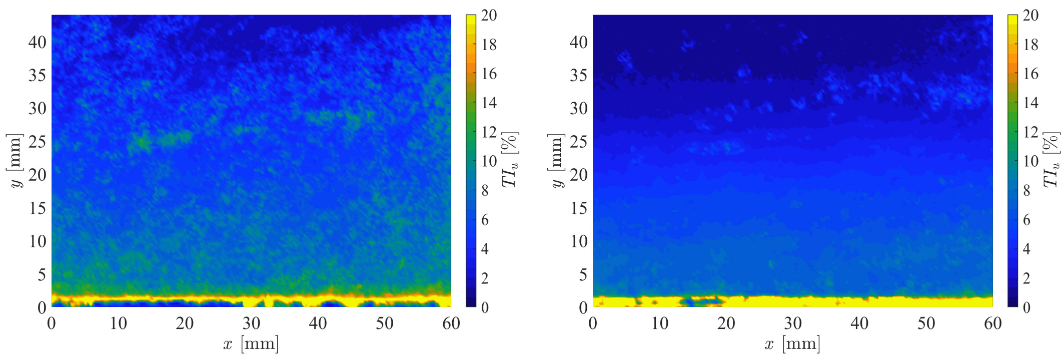

(a) Case $U_\infty \approx 15$ m/s (b) Case $U_\infty \approx 30$ m/s

Figure 6.9: Turbulence intensity of the streamwise velocity component in the FOV for $U_\infty \approx 15$ m/s (a) and $U_\infty \approx 30$ m/s (b).

The colormaps obtained are therefore promising for a future PIV campaign. However, PIV measurements usually struggle to find reliable velocity profiles in the region near the wall, especially in the viscous sublayer. This is due to the difficulty to find a proper cross-correlation function in the interrogation windows near the wall. In order

f_{fan} [Hz]	x [mm]	U_e [m/s]	δ [mm]
	0	15.076	33.478
8	30	15.148	32.605
	60	15.146	32.972
	0	30.888	26.543
16	30	31.068	27.599
	60	31.039	27.783

Table 6.1: External velocity U_e and boundary layer thickness δ of three streamwise positions from the FOV in station 1 for the two operating points of interest.

to evaluate the reliability of the data acquired, it is therefore opportune to extract the velocity profiles and compare with the non-dimensional velocity profiles of the literature. According to Van de Wyer et al. [2], the TBL velocity profile over a smooth flat plate with ZPG is in agreement with the $1/7^{\text{th}}$ power law, expressed in Equation (4.4). By comparing the power law with the extractions of the PIV velocity profiles, the reliability of the data acquired can be evaluated.

In the present work, three streamwise positions have been chosen from the FOV for the analysis: $x = 0$ mm, $x = 30$ mm and $x = 60$ mm. For each position, external velocity U_e and boundary layer thickness δ have been obtained. The results of the parameters are listed in Table 6.1, while the comparison of mean streamwise velocity profiles with the $1/7^{\text{th}}$ power law is shown in Figure 6.10 for the two operating points of interest.

Both cases show the same trend of the power law, but some considerations must be done:

- All the velocity profiles extracted are not exactly null at the wall position. As the physics of the boundary layer imposes a zero velocity at the wall, this behaviour is clearly spurious and remarks the limitation of PIV measurements in the wall region. For a future PIV campaign, the velocity profiles in the very-near region to the wall must be fitted by imposing a zero velocity at $y = 0$ mm.

- The agreement with the power law is approximative for y/δ values up to around 0.5. The discrepancy may be caused by the black paperboard placed on the bottom wall, which increase the surface roughness. As the power law is meant to be used for smooth flat plates, the agreement can be imprecise for rough walls. For this reason, further investigations with other solutions for light reflection will be needed to properly evaluate the reliability of the PIV velocity profiles in the region near the wall.

- Another possible reason for the approximative agreement with the power law may be the choice of the interrogation window shape during the post-processing. Indeed, a square shape is not the best fit for velocity measurements near the wall because strong velocity gradients are present in this region, and thus a wider window height corresponds to a wider range of velocities that increase rapidly. The averaged velocity vector of the interrogation window can be therefore affected by this problem. For this reason, further investigations with other choices of the window shape are recommended for PIV velocity measurements near the wall.

In conclusion, the preliminary PIV campaign proves to be successful and promising for future measurements. The experimental set-up proves to be suitable for the WAABLIEF facility, and the preliminary results obtained are encouraging. However, further investigations and improvements will be necessary to perform a future PIV campaign.

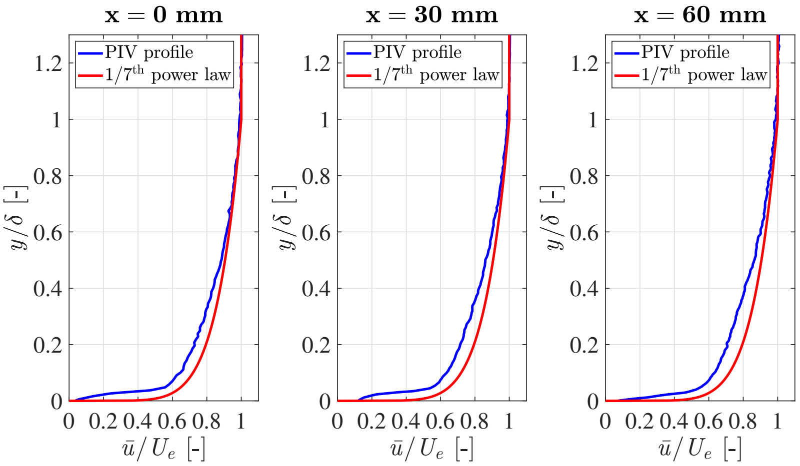

(a) Case $U_\infty \approx 15$ m/s

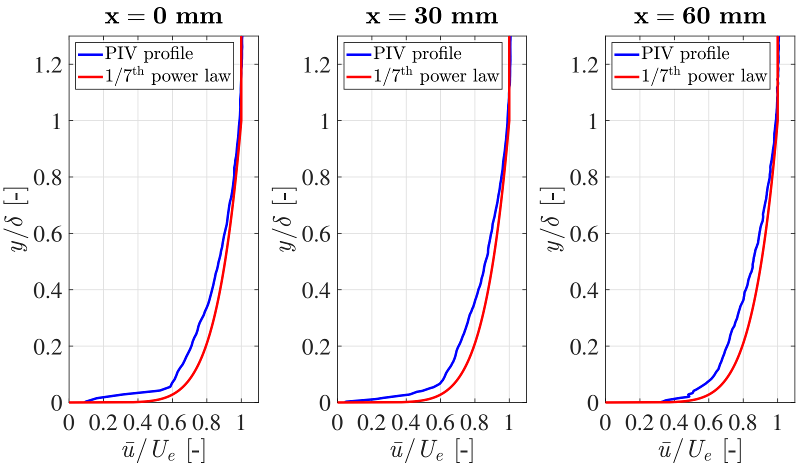

(b) Case $U_\infty \approx 30$ m/s

Figure 6.10: Mean streamwise velocity profiles of three streamwise positions from the FOV in station 1 for $U_\infty \approx 15$ m/s (a) and $U_\infty \approx 30$ m/s (b), compared with the $1/7^{\text{th}}$ power law.

Chapter 7

Conclusions and future work

7.1 Conclusions

An experimental characterization of the turbulent boundary layer over a flat plate under zero pressure gradient has been conducted in the WAABLIEF facility of the von Karman Institute for Fluid Dynamics. The aim of the project is to study the trend of the WPS in a turbulent boundary layer, in order to improve the physical understanding of the interaction between the grazing flow and the solid surface, and enrich the existing database in literature to promote the validation and improvement of statistical models of wall-pressure fluctuations. These models require the knowledge of the TBL parameters, therefore velocity measurements were necessary as much as wall-pressure measurements for the final purpose of the present work.

The experimental campaign included velocity and wall-pressure measurements in station 2 of the test section by means of hot-wire anemometry and microphone-array measurements, respectively. The inlet velocity of the test section has been measured by using a Pitot probe, but also another alternative strategy has been proposed. Moreover, an innovative calibration procedure for the microphone array has been proposed and analyzed in this study.

The results of the hot-wire measurements remarked a development of a fully turbulent boundary layer over the antenna placed in station 2, which is in agreement with the previous works in WAABLIEF facility. In particular, the fair agreement with the theoretical laws for the velocity profiles proves the success of this experimental campaign. However, some problems occurred during the measurements, which may be attributed to blockage and total pressure loss caused by the hot-wire system mounted downstream of station 2. For this reason, only the most reliable case has been considered for WPS normalization, that is the case at $U_\infty \approx 15$ m/s. Further investigations will be needed to properly identify and solve the problem.

The calibration procedure for the microphone array has been analyzed in detail in the present work. First, a parametric study has been conducted in order to find the calibration input signal that leads to the best transfer function possible. After the final input signal has been chosen, the elaboration of the final transfer function has been explained. After some arrangements to remove the evident wiggles due to the calibrator geometrical configuration, the resulting transfer functions proved to be very good for WPS computation. Moreover, the necessity of daily dynamic calibration has been highlighted, as the variability of the tranfer functions over the days is present.

The results obtained for wall-pressure measurements remarked that all the spectra for the different points of interest display a canonical trend. The inner-scale normalization for $U_\infty \approx 15$ m/s turned out to be in fair agreement with the ω^{-5} power law in the high-frequency range, while the outer-scale normalization has shown a good fit with Goody's model, especially in the low- and mid-frequency range. The WPS prediction shown in the present work is therefore very promising for other flow configurations that can be studied in future works. Regarding the cross-coherence, an exponential decay both in spatial and frequency domain have been found, which is an expected result. Moreover, an overestimation of Corcos' model for the spatial decay in the case $U_\infty \approx 15$ m/s at $f = 1000$ Hz can be observed, but the model prediction can be surely improved by analyzing more flow conditions and other parameters, such as convection velocity or coherence length.

In addition to the official experimental campaign, preliminary PIV measurements have been conducted in station 1 of the WAABLIEF facility. The aim of this work is to explore the feasibility of performing such technique in WAABLIEF facility and evaluate the reliability of the data acquired. As PIV measurements expands the information of the velocity field over the antenna, it is therefore interesting to study the possibility of a future PIV campaign in the facility. The main problem encountered during the preliminary campaign concerns the seeding uniformity along the test section, but a quite good set-up solution has been found by using a mixing box with a homemade turbulence grid added at the outlet. The results of the colormaps and velocity profiles extractions exhibited a coherent and uniform velocity field that is in line with the typical trend of a velocity profile in a TBL, remarking the successful and promising features of this preliminary campaign. The PIV measurements can be therefore considered feasible to perform a future campaign. However, further investigations will be necessary to find a better solution for light reflection and a better choice of the interrogation window shape, as they can affect the reliability of the results.

7.2 Recommendations for future work

The present work has led to interesting results, which are encouraging for future improvements of the experimental campaign. In particular, some ideas and suggestions for the future have emerged:

- A proper solution for the static calibration procedure of the hot-wire system must be found. The best solution is to find a way to calibrate the hot-wire sensor directly with the wind tunnel flow, as it is the velocity field to measure. This solution can be performed by using a Pitot probe mounted in station 2, in order to measure the same velocity sensed by the hot-wire in wind tunnel.

- Future improvements are needed to solve the discrepancy between the velocity fields during hot-wire and wall-pressure measurements. The easiest solution is to perform simultaneously the hot-wire and wall-pressure measurements, or at least with the same facility configuration, i.e. with the hot-wire system mounted. However, a proper investigation about the velocity discrepancy is necessary to definitively solve the problem and allow flow measurements with the highest velocities possible in WAABLIEF facility.

- A modification of the calibrator device may be a winning solution to solve the destructive interference at the calibrator microphone port. Indeed, with another lateral port at 90° from the present one, the resonance frequency may be avoided for that radial position. By using a mixed calibration with two microphone signals coming from two lateral ports placed at 90°, the mixed calibration strategy could be even more effective.

- A background noise reduction for the channels of the electret amplifier is needed, in order to have the possibility to acquire simultaneously the signals of all the 16 electret microphones of the L-shaped array.

- A proper solution to avoid light reflections over the antenna during PIV measurements is necessary to properly characterize the real flow field over the antenna. One solution may be to paint the antenna black or to use another auxiliary black flat plate with the same roughness of the real antenna.

- Another improvement for the PIV measurements can be a more reasonable choice of the interrogation window size during the post-processing. By using a rectangular window shape in the wall region, with the long edge parallel to the wall, the wall-normal direction has a better spatial resolution while having the same tracer particles of the square window, as the long edge of the rectangular shape includes more particles in streamwise direction. With this solution, the velocity field computation near the wall is more suitable for the velocity gradients.

Bibliography

[1] von Karman Institute for Fluid Dynamics. *About VKI.* von Karman Institute for Fluid Dynamics Official Website, URL: https://www.vki.ac.be/index.php/about-vki#about-vki.

[2] N. Van de Wyer, A. Zapata, D. Nogueira, C. Schram. *Development of a test rig for the measurement of turbulent boundary layer wall pressure statistics.* In 2018 AAIA/CEAS Aeroacoustics Conference, American Institute of Aeronautics and Astronautics, Atlanta, Georgia, June 2018.

[3] K. Kestel. *Database Generation for Turbulent Boundary Layer Wall Pressure Spectra Under Pressure Gradients.* VKI Research Master Report, von Karman Institute for Fluid Dynamics, 2020.

[4] H. Schlichting, K. Gersten. *Boundary-Layer Theory.* Springer-Verlag Berlin Heidelberg, 2017.

[5] E. H. Bani-Hani, M. E. H. Assad. *Boundary-Layer Theory of Fluid Flow past a Flat-Plate: Numerical Solution using MATLAB.* International Journal of Computer Applications (0795-8887), Volume 180 - No. 18, February 2018.

[6] T. L. Bergman, A. S. Lavine, F. P. Incropera, D. P. Dewit. *Fundamentals of heat and mass transfer.* John Wiley & Sons, seventh Edition, pp. 389-391, 2011.

[7] F. H. Clauser. *The Turbulent Boundary Layer.* Academic Press Inc., Johns Hopkins University, Baltimore, Maryland, 1956.

[8] A. Zapata. *Measurement and modelling of turbulent wall pressure in a boundary layer.* VKI Research Master Report, von Karman Institute for Fluid Dynamics, 2017.

[9] J. P. Crimaldi. *Turbulence structure of velocity and scalar fields over a bed of model bivalves.* PhD Thesis, Stanford University, 1998.

[10] G. Degrez. *Two-dimensional boundary layers - Revised edition.* VKI-CN 143, von Karman Institute for Fluid Dynamics, 2013.

[11] D. B. Spalding. *A Single Formula for the "Law of the Wall".* Journal of Applied Mechanics, September 1961.

[12] D. Coles. *The law of the wake in the turbulent boundary layer*. Guggenheim Aeronautical Laboratory, California Institute of Technology, Pasadena, January 1956.

[13] M. Barcan, I. Chirica, E. F. Beznea. *Numerical Vibro-Acoustic Analysis of a Ship Compartment Structure*. ITM Web of Conferences 29:02015, "Dunărea de Jos" University of Galati, Romania, January 2019.

[14] S. W. Rienstra, A. Hirschberg. *An Introduction to Acoustics*. Eindhoven University of Technology, November 2019.

[15] J. Anthoine, T. Arts, H. L. Boerrigter, J.-M. Buchlin, M. Carbonaro, G. Degrez, R. Dénos, D. Fletcher, D. Olivari, M. L. Riethmuller, R. A. Van den Braembussche. *Measurement Techniques in Fluid Dynamics - An Introduction*. VKI Lecture Series 1994-01, 3rd revised edition, von Karman Institute for Fluid Dynamics, 2009.

[16] Y. F. Hwang, W. K. Bonness, S. A. Hambric. *Comparison of semi-empirical models for turbulent boundary layer wall pressure spectra*. Journal of Sound and Vibration 319, pp. 199-217, 2009.

[17] M. Goody. *Empirical Spectral Model of Surface Pressure Fluctuations*. AIAA Journal, Vol. 42, No. 9, September 2004.

[18] A. V. Smol'yakov. *Calculation of the spectra of pseudosound wall pressure fluctuations in turbulent boundary layers*. Acoustical Physics 46 (3), 2000.

[19] M. S. Howe. *Acoustics of Fluid-Structure Interactions*. Cambridge University Press, Cambridge, England, U.K., 1998.

[20] D. M. Chase. *Modeling the Wavevector-Frequency Spectrum of Turbulent Boundary Layer Wall Pressure*. Journal of Sound and Vibration, Vol. 70, No. 1, pp. 29-67, 1980.

[21] G. M. Corcos. *The structure of the pressure field in boundary-layer flows*. Journal of Fluid Mechanics, Vol. 18, pp. 353-378, 1964.

[22] C. Schram, N. Van de Wyer. *An optimized microphone array for the measurement of turbulent boundary layer wall pressure wavenumber-frequency spectra*. In 2018 AAIA/CEAS Aeroacoustics Conference, American Institute of Aeronautics and Astronautics, Atlanta, Georgia, June 2018.

[23] W. Blake. *Mechanics of flow-induced sound and vibration*. Academic Press, Vol. II, New York, 1986.

[24] A. V. Smol'yakov. *A New Model for the Cross-Spectrum and Wavenumber-frequency Spectrum of Turbulent Pressure Fluctuations in a Boundary Layer*. Acoustical Physics, Vol. 52, No. 3, pp. 331-337, 2006.

[25] Brüel & Kjær. *Product Data: Sound Calibrator Type 4231*. Brüel & Kjær Official Website, URL: https://www.bksv.com/-/media/literature/Product-Data/bp1311.ashx.

[26] M. Raffel, C. E. Willert, F. Scarano, C. J. Kähler, S. T. Wereley, J. Kompenhans. *Particle Image Velocimetry: A Practical Guide*. Springer International Publishing AG, third edition, 2018.